



저작자표시-비영리-변경금지 2.0 대한민국

이용자는 아래의 조건을 따르는 경우에 한하여 자유롭게

- 이 저작물을 복제, 배포, 전송, 전시, 공연 및 방송할 수 있습니다.

다음과 같은 조건을 따라야 합니다:



저작자표시. 귀하는 원저작자를 표시하여야 합니다.



비영리. 귀하는 이 저작물을 영리 목적으로 이용할 수 없습니다.



변경금지. 귀하는 이 저작물을 개작, 변형 또는 가공할 수 없습니다.

- 귀하는, 이 저작물의 재이용이나 배포의 경우, 이 저작물에 적용된 이용허락조건을 명확하게 나타내어야 합니다.
- 저작권자로부터 별도의 허가를 받으면 이러한 조건들은 적용되지 않습니다.

저작권법에 따른 이용자의 권리는 위의 내용에 의하여 영향을 받지 않습니다.

이것은 [이용허락규약\(Legal Code\)](#)을 이해하기 쉽게 요약한 것입니다.

[Disclaimer](#)

이학석사 학위논문

Au-Ag 코어-셸 나노로드에서 굴절률  
감도 및 화학적 계면 감쇠의 효과

The Effects of Refractive Index Sensitivity and  
Chemical Interface Damping in Au-Ag Core-Shell

울산대학교 대학원

화학과

류경림

The Effects of Refractive Index  
Sensitivity and Chemical Interface  
Damping in Au–Ag Core–Shell

지도교수 하 지 원

이 논문을 이학석사학위 논문으로 제출함

2021년 02월

울산대학교 대학원

화학과

류경림

류경림의 석사학위 논문을 인준함

심사위원 하지원 (인)

심사위원 이영일 (인)

심사위원 홍종욱 (인)

울산대학교 대학원

2021년 02월

## 국문 초록

금, 은, 구리와 같은 귀금속 나노 입자는 국지 표면 플라즈몬 공명 (Localized Surface Plasmon resonance, LSPR) 현상에 의해 그들의 모양, 크기, 주변 매질의 굴절률(Refractive Index, RI) 등에 따라 독특한 광학적 특성을 가지며 그로 인해 다양한 분야에서 응용되고 있다. 그 중에서 금 및 은 나노 입자는 LSPR 바이오 센싱과 관련하여 가장 매력적인 물리적 특성을 보여준다. 금 나노 입자는 높은 화학적 안정성과 생체 적합성을 나타내므로 많은 분야에서 응용되고 있다. 은 나노 입자는 주어진 모양과 크기에 대해 금 나노 입자와 비교할 때 더 나은 RI 감도를 제공한다. 그럼에도 불구하고 은 나노 입자는 열등한 화학적 안정성 및 생체 적합성으로 인해 LSPR 기반 바이오 센싱 응용 분야에 사용될 때 수많은 한계를 보이는 것으로 되었지만, 최근에는 은 나노 입자와 금의 조합으로 많은 개선이 이루어졌다. 예를 들어, 금과 은을 혼합하여 합금 또는 Au-Ag 코어-셸 나노 입자 (AuNRs @ Ag, core @ shell) 를 형성하면 Au-Ag 비율을 제어하여 지속적으로 조정할 수 있는 하이브리드 LSPR 밴드가 생성된다.

본 연구에서는 암시야(Dark-Field, DF) 현미경, 자외선-가시광선 분광기(UV-VIS spectroscopy), 표면증강라만산란(Surface Enhanced Raman

Scattering, SERS), 주사 전자 현미경(Scanning Electron Microscope, SEM)을 사용하여 AuNRs@Ag의 광특성을 분석하였다. 첫째, 셸 두께가 다른 AuNRs@Ag에서 피리딘 유도체의 흡착 배향에 따른 화학적 계면 감쇠(Chemical Interface Damping, CID) 효과에 대해 알아보았다. 전자공여기를 갖는 피리딘 유도체는 단일 AuNRs@Ag에 흡착되어 질소와 은 표면의 상호 작용을 통해 강한 CID 효과를 유도하였다. AuNRs@Ag 두꺼운 은 셸의 경우 모든 피리딘 유도체에 대해 얇은 은 셸을 사용하는 AuNRs@Ag에 비해 상당히 향상된 CID 효과를 나타냈다. 피리딘 분자의 높은 기율기와 달리 electron donating group(EDG)을 포함하는 피리딘 유도체는 표면증강라만산란 및 동적 광산란 측정에 따라 Ag 표면에 평행한 배향을 채택하여 Ag 표면에서 피리딘과는 다른 표면 커버리지를 생성하고 LSPR 선폭확장이 감소됨을 확인하였다. 둘째, 금 코어의 크기는 같고 은 셸의 두께가 다른 두가지의 AuNRs@Ag를 사용하여 주변 매질 굴절률에 따른 민감도(Refractive Index Sensitivity, RIS)에 은 셸의 두께에 따른 영향을 알아보고 2차 미분에 의한 변곡점을 이용하여 RIS를 향상시켰다. 따라서 본 연구는 단일 AuNRs@Ag에서 피리딘 유도체의 공여 치환기와 Ag 셸 두께가 CID에 미치는 영향에 대한 보다 깊은 이해를 제공하고 은 셸 두께 증가로 인한 LSPR 센서의 개선을 보여준다.

## English Abstract

Noble metal nanoparticles such as gold, silver, and copper have unique optical properties depending on their shape, size, and refractive index (RI) of the surrounding medium due to a localized surface plasmon resonance (LSPR) phenomenon. Among metallic NPs, gold (Au) and silver (Ag) nanoparticles (NPs) have demonstrated the most fascinating physical properties with regard to LSPR biosensing. These gold nanoparticles have been applied in many fields because they have the advantages of being biocompatible, having high chemical stability and easy surface modification. However, for a given shape and size, AgNPs provide better RI sensitivity when compared with AuNPs. Nevertheless, AgNPs have been reported to show numerous limitations when utilized for LSPR-based biosensing applications due to their inferior chemical stability and biocompatibility. Recently, many improvements have been achieved with the combination of AgNPs with Au. For instance, mixing Au and Ag to form either alloys or Au–Ag core–shell NPs (AuNRs@Ag, core @ shell) results in a hybrid LSPR band which can be tailored continuously by controlling the Au–Ag ratio.

In this study, we used Dark-Field (DF) microscopy, UV-Vis spectroscopy (UV-Vis), Surface Enhanced Raman Scattering (SERS) and Scanning Electron Microscope (SEM) to analyze the optical properties of single AuNRs@Ag. First, the effects of chemical interface damping (CID) according to adsorption orientation of pyridine derivatives in AuNRs@Ag with different shell thicknesses were investigated.

Pyridine derivatives having electron-donating groups (EDGs) were adsorbed on single AuNRs@Ag and induced a strong CID through the interaction of nitrogen with the Ag surface. AuNRs@Ag with thick shells showed a considerably enhanced CID effect compared with AuNRs@Ag with thin shells for all pyridine derivatives. In contrast to the high inclination of pyridine molecules, pyridine derivatives bearing EDGs adopted a parallel orientation to the Ag surface according to surface-enhanced Raman spectroscopy and dynamic light scattering measurements, which resulted in different surface coverage on the Ag surface and decreased LSPR linewidth broadening. Second, two AuNRs@Ag with the same size of the gold core and different thickness of the silver shell were used to investigate the effect of the thickness of the silver shell on the RI sensitivity according to the refractive index of the surrounding medium. RI sensitivity was improved by using the inflection point by the second derivative. Therefore, this study provides a deeper understanding of the effect of the donor substituent of the pyridine derivative and the Ag shell thickness on CID in a single AuNRs@Ag, and shows the improvement of the LSPR sensor due to the increase in silver shell thickness.

## Index

Korean abstract.....	I
Abstract .....	III
Figure index .....	VII
Scheme index .....	X
Table index.....	XI
<b>1. Introduction .....</b>	<b>1</b>
1.1. Metallic Nanoparticles (NPs) .....	1
1.2. Chemical Interface Damping (CID) .....	2
1.3. Surface-Enhanced Raman Scattering (SERS) .....	5
1.4. Inflection Point of LSPR Peak. ....	6
1.5. Objectives of Study .....	8
<b>2. Experimental section.....</b>	<b>10</b>
2.1. Materials and Chemicals .....	10
2.2. Sample Preparation and Characterization .....	10

2.3. Single Particle Microscopy and Spectroscopy .....	11
2.4. Raman and SERS measurements.....	12
<b>3. Results and discussion.....</b>	<b>16</b>
3.1. Influence of the Preferred Orientation of Pyridine Derivatives with Donor Substituents on Chemical Interface Damping Induced in Silver-Coated Gold Nanorods with Different Shell Thicknesses .....	16
3.2. Influence of shell thickness on the refractive index sensitivity of localized surface plasmon resonance inflection points in silver-coated gold nanorods ...	41
<b>4. Conclusions .....</b>	<b>53</b>
<b>5. Reference.....</b>	<b>55</b>

## Figure index

- Figure 1. A photograph to show the experimental setup for single particle DF spectroscopy and Raman spectroscopy (back-side)..... 14
- Figure 2. (A,B) Schematic diagram showing the dimensions of AuNRs@Ag with two different Ag shell thicknesses. (C,D) TEM images of (C) thick AuNRs@Ag and (D) thin AuNRs@Ag. The Au core and Ag shell are clearly observed in the TEM images..... 18
- Figure 3. Energy dispersive spectroscopy data of AuNRs@Ag with thick shell thicknesses ..... 19
- Figure 4. Energy dispersive spectroscopy data of AuNRs@Ag with thin shell thicknesses.....20
- Figure 5. (A, B) UV-Vis extinction spectra of (A) thick AuNRs@Ag in water and (B) thin AuNRs@Ag dispersed in water.....21
- Figure 6. (A) Schematic diagram showing the chemical structure of pyridine, 4-AP, and 4-DMAP used as adsorbates. (B) Schematic diagram showing the adsorption of pyridine on the Ag surface through nitrogen–Ag interaction. (C) Schematic diagram showing the CID mechanism for the transfer of hot electrons generated in AuNRs@Ag to the empty orbitals (LUMOs) of adsorbates.....23
- Figure 7. (A,B) DF scattering images of (A) thick AuNR@Ag1 and (B) thin AuNR@Ag1. (C,D) Single-particle scattering spectra of (C) thick AuNR@Ag1 and (D) thin AuNR@Ag1. The experimental spectrum (blue curve) is fitted well by the Lorentzian function (green curve) .....25
- Figure 8. (A–D) Single-particle scattering spectra of (A) thick AuNR@Ag upon removal of CTAB (bare), (B) thick AuNR@Ag after the adsorption of pyridine on the surface, (C) thick AuNR@Ag with 4-AP, and (D) thick AuNR@Ag with 4-DMAP. (E–H) Single-particle scattering spectra of (E) thin AuNR@Ag upon removal of CTAB (bare), (F) thin AuNR@Ag after the adsorption of pyridine on the surface, (G) thin AuNR@Ag with 4-AP, and (H) thin AuNR@Ag with 4-DMAP.....28
- Figure 9. Normalized scattering spectra of single AuNRs (on average, 25 nm×73 nm) without Ag shell. The average LSPR wavelength and linewidth were determined to be 1.71 eV and 96.1 meV, respectively..... 29
- Figure 10. Normalized scattering spectra of single AuNRs (on average, 25 nm×73 nm)

upon adsorption of pyridine. The average LSPR wavelength and linewidth were determined to be 1.62 eV and 109.3 meV, respectively.....30

Figure 11. (A) Change in the scattering spectrum of thick AuNR@Ag after the adsorption of pyridine molecules. (B) Change in the scattering spectrum of thin AuNR@Ag after the adsorption of pyridine molecules. The scattering spectra were red-shifted for both thick AuNR@Ag and thin AuNR@Ag after the adsorption of pyridine molecules on the particle surface.....31

Figure 12. (A,B) Comparison of the fwhm values of AuNRs@Ag for bare, pyridine, 4-AP, and 4-DMAP adsorbates under the same experimental conditions. The error bars are based on the determination of the standard deviation measured from ~ 150 nanoparticles for each sample.....33

Figure 13. (A) Schematics showing the preferred orientation of pyridine and pyridine derivatives with EDGs (4-AP and 4-DMAP). The pyridine molecule is adsorbed onto the Ag surface through a strong nitrogen–Ag interaction. (B) Bulk Raman (top) and SERS (bottom) spectra for 4-AP. (C) Bulk Raman (top) and SERS (bottom) spectra for 4-DMAP. In this study, thin AuNRs@Ag were used for SERS measurements at 785 nm.....38

Figure 14. (A-C) Dynamic light scattering (DLS) measurements of thick AuNRs@Ag (48 nm×90 nm) with (A) CTAB, (B) pyridine and (C) 4-AP as adsorbates. The change of the particle size of AuNRs@Ag, measured by a DLS measurement. In case of 4-AP, the mean size decreased to 268.9 from 281.2 as compared to that of pyridine.....39

Figure 15. (A) Bulk Raman and (B) SERS spectra for pyridine. In this study, thin AuNRs@Ag (28 nm × 78 nm) were used for SERS measurement at 785-nm excitation.....40

Figure 16. (A) Dark-field image of single Ag@AuNRs with thick Ag shell. (B) Corresponding scattering spectra of single Ag@AuNRs with thick Ag shell squared with green in (A). (C) Dark-field image of single Ag@AuNRs with thin Ag shell. (D) Corresponding scattering spectra of single Ag@AuNRs with thin Ag shell squared with yellow in (C) .....42

Figure 17. (A) Change in the LSPR scattering spectra of single Ag@AuNRs with thick Ag shell in the different local RI media, air, water, oil. (B) Change in the LSPR scattering spectra of single Ag@AuNRs with thin Ag shell in the different local RI media, air, water, oil. (C) LSPR wavelength shifts for thick Ag@AuNRs (blue-curve) and thin Ag@AuNRs (red-curve) as a function of the local RI of medium. (D) Comparison of RI sensitivity at the maximum LSPR wavelength for thick Ag@AuNRs (left) and thin Ag@AuNRs (right) .....44

Figure 18. Inflection point method for single particle LSPR scattering sensing with Ag@AuNRs with thick Ag shell thickness in the three local refractive indexes (air, water, and oil). (A–C) LSPR scattering efficiencies (first row), LSPR scattering efficiencies first order derivatives (second row), and LSPR scattering efficiencies second order derivatives (third row). (D) Peak energy plotted against the three local RI for A, B, and C. (E) Sensitivity of local RI media on peak shifts A, B and C.....46

Figure 19. Inflection point method for single particle LSPR scattering sensing with Ag@AuNRs with thin Ag shell thickness in the three local refractive indexes (air, water, and oil). (A–C) LSPR scattering efficiencies (first row), LSPR scattering efficiencies first order derivatives (second row), and LSPR scattering efficiencies second order derivatives (third row). (D) Peak energy plotted against the three local RI for A, B, and C. (E) Sensitivity of local RI media on peak shifts A, B and C.....50

## **Scheme index**

**Scheme 1.** Schematic diagram showing the working principle of scattering-based DF microscopy and spectroscopy.....14

**Scheme 2.** Experimental setup for surface-enhanced Raman spectroscopy.....15

## Table index

Table 1. Inflection points and LSPR peak locations on the curvatures of single Ag@AuNRs with thick Ag shell thickness in refractive index of air.....	48
Table 2. Inflection points and LSPR peak locations on the curvatures of single Ag@AuNRs with thick shell thickness in refractive index of water.....	48
Table 3. Inflection points and LSPR peak locations on the curvatures of single Ag@AuNRs with thick shell thickness in refractive index of oil.....	48
Table 4. Inflection points and LSPR peak locations on the curvatures of single Ag@AuNRs with thin shell thickness in refractive index of air.....	52
Table 5. Inflection points and LSPR peak locations on the curvatures of single Ag@AuNRs with thin shell thickness in refractive index of water.....	52
Table 6. Inflection points and LSPR peak locations on the curvatures of single Ag@AuNRs with thin shell thickness in refractive index of oil.....	52

# 1. Introduction

## 1.1. Metallic Nanoparticles (NPs)

Metallic nanoparticles (NPs) show distinct optical properties which are sensitive to their shapes, sizes and refractive index (RI), caused by the localized surface plasmon resonance (LSPR) effect.<sup>1-4</sup> When metallic NPs are irradiated, the conduction electrons on their surfaces are excited and collectively oscillate with the incident electromagnetic field. Furthermore, the strong interaction between metallic NPs causes light to be confined into sub-diffraction volumes.<sup>5</sup> For many years, the optical properties of single metallic NPs have been intensively investigated by far-field single particle imaging and spectroscopic techniques, such as scattering-based dark-field microscopy and absorption-based photothermal imaging, without ensemble averaging.<sup>6-8</sup> It has been reported that the LSPR of metallic NPs is strongly dependent on the three-dimensional (3D) structure and size of the nanoparticles, as well as on the RI of the surrounding medium.<sup>2,9</sup> Accordingly, by controlling these parameters, it is possible to tune the characteristic plasmonic properties for specific purposes and applications.<sup>4,10</sup> Therefore, in the previous few decades, LSPR in metallic NPs has been widely utilized in applications pertaining to chemical and biological sensors.<sup>11-13</sup> LSPR-based biosensing is based on the sensitivity of the LSPR wavelength to

variations in local RI around the nanoparticle surface. The refractive index sensitivity (RIS) aids to measure the displacement in the wavelength shift of the LSPR peak.

Among metallic NPs, gold (Au) and silver (Ag) nanoparticles have demonstrated the most fascinating physical properties with regard to LSPR biosensing.<sup>14, 15</sup> AuNPs show good chemical stability and biocompatibility,<sup>16, 17</sup> and so they are studied to a large extent in sensing and surface-enhanced Raman scattering (SERS) applications.<sup>18-20</sup> However, for a given shape and size, AgNPs provide better RI sensitivity when compared with AuNPs.<sup>21-23</sup> Nevertheless, AgNPs have been reported to show numerous limitations when utilized for LSPR-based biosensing applications due to their inferior chemical stability and biocompatibility.<sup>24</sup> Recently, many improvements have been achieved with the combination of AgNPs with Au. For instance, mixing Au and Ag to form either alloys or Au–Ag core–shell NPs results in a hybrid LSPR band which can be tailored continuously by controlling the Au–Ag ratio.<sup>13, 21</sup>

## **1.2. Chemical Interface Damping (CID)**

It is essential to understand plasmon damping processes in gold nanoparticles for their efficient use in various photochemical reactions.<sup>25, 26</sup> To date, plasmon relaxation pathways in gold nanoparticles of various sizes and shapes have been mainly investigated by ultrafast spectroscopy techniques. However, such ultrafast

techniques are expensive and inconvenient.<sup>27</sup> Fortunately, the measurement of LSPR spectrum linewidth using only single gold nanoparticles allows overcoming the timescale limitation of ultrafast techniques.<sup>28-30</sup> Given the proportional relationship between the LSPR linewidth and the damping rate, the homogeneous LSPR linewidth and the detailed picture of the total LSPR damping pathways can be revealed by using far-field single-particle spectroscopy techniques.<sup>31</sup> Among the several far-field spectroscopy techniques available, scattering-based dark-field (DF) microscopy and spectroscopy have been mainly employed to reveal the homogeneous LSPR linewidth broadening in single gold nanoparticles.<sup>29, 32-35</sup> The LSPR linewidth is governed by various plasmon decay channels including bulk metal damping ( $\Gamma_{\text{bulk}}$ ), electron-surface scattering ( $\Gamma_{\text{surf}}$ ), radiation damping ( $\Gamma_{\text{rad}}$ ), and chemical interface damping (CID) ( $\Gamma_{\text{CID}}$ ).<sup>26, 30, 34, 36-40</sup> Therefore, the LSPR total damping channel can be described by the following equation.(1)

$$\Gamma_{\text{tot}} = \Gamma_{\text{bulk}} + \Gamma_{\text{rad}} + \Gamma_{\text{surf}} + \Gamma_{\text{CID}} \quad (1)$$

Among these decay processes, CID is the most recently proposed damping pathway.<sup>26, 41-43</sup> CID occurs when strongly interacting molecules are adsorbed on the nanoparticle surface, which induces the direct transfer of hot electrons generated in Au to the empty orbitals of the adsorbates (lowest unoccupied molecular orbitals or LUMOs).<sup>44-48</sup> Furthermore, in the case of CID, the electron transfer from the electronic

states of the adsorbate into Au is also possible.<sup>49</sup> Recent studies on CID have used single-particle spectroscopy to reveal the homogeneous LSPR linewidth of single gold nanorods (AuNRs) at the single-particle level.<sup>36, 37, 47, 50</sup> However, our understanding of CID is still very limited.<sup>36</sup> For example, such recent CID studies were mostly conducted using thiol ( $-SH$ ) molecules, which have a strong binding affinity for AuNRs. In addition, we have recently reported a study on CID induced by pyridine molecules bearing nitrogen substituents, which led to LSPR linewidth broadening in single AuNRs through the Au–nitrogen interaction.<sup>51</sup> However, the effect of pyridine derivatives with nitrogen and different substituents on CID in Ag-coated AuNRs (AuNRs@Ag, core@shell) is unknown. More specifically, the influence of the preferred orientation of pyridine derivatives with donor substituents on CID is unanswered so far. Moreover, another interesting topic arises from plasmon decay channel by interfaces, both the Au–Ag interface and the medium–Ag interface in single AuNRs@Ag.<sup>52</sup> However, our understanding on the additional plasmon damping associated with the Au–Ag interface and the silver shell coating is still limited. It is also unknown how the Ag shell thickness can affect the LSPR linewidth broadening (or CID) in AuNRs@Ag with various shell thicknesses. Thus, it is essential to perform single-particle studies to answer the abovementioned questions and to gain a deeper insight into the effects of pyridine derivatives and the Ag shell thickness on plasmon damping and CID in Au–Ag core–shell nanoparticles.

### 1.3. Surface-Enhanced Raman Scattering (SERS)

Raman spectroscopy is an important analytical technique capable of providing vibration-level molecular information through structural fingerprinting. However, Raman spectroscopy also has a fatal drawback of poor reproducibility because the signal is very weak, it is a kind of inelastic scattering, and spontaneous scattering is almost 0.0001% of the radiation. Various techniques have been developed including surface-enhanced Raman scattering (SERS) to overcome these drawbacks of Raman spectroscopy. SERS is a phenomenon that can significantly enhance the signal by adsorbing target molecules (called probe molecules or Raman reporters) on a metal surface. The first SERS was discovered in 1973 by Martin Fleischmann et al. in pyridine adsorbed on coarse silver.<sup>53</sup> Compared to the normal Raman signal, the degree of improvement of the SERS signal can be expressed as the enhancement factor (EF), and the maximum EF of the published signal is: About 10<sup>14</sup>. SERS has shown great advantages of high selectivity, quenching the fluorescence, and the removal of the photodecomposition of molecules.<sup>54-56</sup>

This simple method for improving Raman spectroscopy, SERS, has been considered an attractive research topic from basic to applied and has been explosively studied to this day. In the case of SERS, there are two complementary mechanisms that have been described for powerful enhancements and have been well documented through numerous studies.<sup>57-60</sup> One is the electromagnetic enhancement (EM) that

focuses on the surface plasmon resonance of metals, usually plasmonic nanoparticles that feature localized surface plasmon resonance (LSPR). To be precise, the enhanced electromagnetic field, which is controlled by the roughness or morphology of the metal nanoparticles, is the main reason for the enhancement. Similarly, the presence of "hot spots", which are very strong local fields created on rough surfaces or interparticle spacing between agglomerated nanoparticles, is key to a strong signal.<sup>61</sup> The other mechanism is the chemical enhancement (CE) related with a charge-transfer between metals and probe molecules. When an adsorbate and metallic nanoparticle form a strong chemical bonding, the metal can act as an intermediate for the excitation of molecules under the condition that the resonance symmetrically between the electric states of molecules and the fermi level of metal.<sup>62, 63</sup>

#### **1.4. Inflection point of LSPR Peak.**

Despite the surprising advantages of LSPR-based biosensors, there are still many fundamental limitations. First, the efficiency of LSPR-based sensor using metallic NPs is lower than that of surface plasmon polariton (SPP) sensor.<sup>64</sup> The precise determination of LSPR properties is influenced by a realistic representation of the wavelength-dependent dielectric function of the nanoparticles.<sup>65</sup> Therefore, simplistic models negatively impact the fundamental quantities that are necessary for the reliable fabrication of plasmonic devices.<sup>66</sup> Second, LSPR biosensors are limited

by the asymmetric expansion of the LSPR peak when measuring changes in the local environment on the nanoparticle surface.<sup>67</sup> Also, the change in the shape of the LSPR peak negatively affects the sensing efficiency.<sup>68</sup> To overcome these limitations, recent studies have used lithographic methods to improve their efficiency, but there are several drawbacks such as high processing cost and low yield.<sup>64</sup> Recently, Chen and colleagues reported a different approach to assessing changes in LSPR curvature of ensemble samples in relation to changes in RI.<sup>64</sup> They showed that higher RI sensitivity was obtained at the inflection point (IF) located on the long wavelength side (or low energy side) of the LSPR extinction peak.<sup>67</sup> However, that report was based on only ensemble samples of Au nanoparticles rather than single nanoparticles. It has been reported that in single Au bipyramids with sharp tips the LSPR IFs present superior RI sensitivity when compared with the LSPR wavelength maximum peak.<sup>69</sup> Nevertheless, to the best of our knowledge, there have been no studies to report the RI sensitivity of LSPR curvatures (or IFs) in single Ag@AuNRs with variation in Ag shell thickness. We therefore investigated how the shell thickness affects the RI sensitivity at LSPR IFs while considering the first and second derivatives of homogeneous scattering spectra of Ag@AuNRs.<sup>69</sup>

## 1.5. Objectives of Study

Firstly, we conducted single-particle scattering studies to reveal the effect of Ag shell thickness on the homogeneous LSPR linewidth broadening of AuNRs@Ag with two different shell thicknesses for the same size of the AuNR core. Furthermore, we investigated how pyridine derivatives having donor substituents affect the CID phenomenon through the Ag–nitrogen interaction. In addition, we demonstrated the preferred orientation of pyridine derivatives with electron-donating groups (EDGs) on the Ag surface compared with that of unsubstituted pyridine, which can directly affect the surface coverage and LSPR linewidth broadening (or CID).

Next, for RI-based LSPR biosensing applications, limited studies have been conducted so far on Au–Ag core–shell NPs by mixing various ratios of Au and Ag. Furthermore, LSPR biosensors are still prone to the occurrence of unsymmetric peak broadening while detecting changes in the local environment at the nanoparticle surface. The unsymmetrical nature of the LSPR peak has the potential to negatively affect sensing efficiency. Recent studies have been conducted to overcome the aforementioned limitation using homogeneous LSPR curvature (or LSPR inflection points, IFs) changes in metallic NPs with respect to local RI changes. There have been no studies, however, to elucidate RI sensitivity at LSPR IFs of single Au nanorod (AuNR) coated with versatile Ag shell thickness (Ag@AuNRs). We studied single particle study was presented to reveal the effect of Ag shell thickness on RI sensitivity

at LSPR IFs of scattering spectra of single Ag@AuNRs. The RI sensing effect of single Ag@AuNRs embedded in three different surrounding media (air, water, and oil) was studied by dark-field (DF) microscopy and spectroscopy.

## **2. Experimental section**

### **2.1. Materials and Chemicals**

Pyridine and pyridine derivatives 4-aminopyridine (4-AP) and 4-dimethylaminopyridine (4-DMAP) were purchased from Sigma-Aldrich (St. Louis, MO, USA). Cetyltrimethylammonium bromide (CTAB)-stabilized AuNRs with an average size of 25 nm × 73 nm were purchased from Nanopartz (Loveland, CO, USA). Furthermore, Ag-coated AuNRs with two different sizes (38 nm × 83 nm, 28 nm × 78 nm) were obtained from Nanoseedz (Hong Kong, China). Microscope cover glasses were obtained from Sigma-Aldrich.

### **2.2. Sample Preparation and Characterization**

Structural characterization was carried out using transmission electron microscopy (TEM, JEL-2100F, JEOL). Furthermore, their LSPR absorption spectra in water were measured under a Varian Cary 100 UV-Vis spectroscope (Agilent, USA). For UV–Vis measurements, bare metallic NPs solutions were used without any dilution. For sample preparation for single-particle spectroscopy, the microscope cover

glasses were cleaned by sonicating in methanol for 15 min, followed by O<sub>2</sub> plasma cleaning for 1 min. The solution containing AuNRs@Ag was 20-fold diluted and sonicated for 3 min to prevent nanoparticle aggregation. A drop of the diluted AuNR@Ag solution was then cast onto the glass slides and allowed to dry. To obtain air surrounding medium condition, we dried solution dropped on slide glass after covering with cover glass because solvent of dropped solution is water. In case of oil medium condition after drying solution in the same method of sample preparation with air condition, immersion oil was dropped. The concentration of AuNRs@Ag deposited on the glass surface was adjusted to be about 1  $\mu\text{m}^{-2}$  in order to characterize single AuNRs@Ag more conveniently and to minimize the interparticle LSPR coupling that results in spectral shift.

### **2.3. Single Particle Microscopy and Spectroscopy**

In this study, DF microscopy imaging was used under a Nikon inverted microscope (ECLIPSE Ti-U). The schematic and real instrument were presented in scheme 1, figure 1. In DF mode, the microscope utilized a Nikon Plan Fluor 100 $\times$  0.5–1.3 oil iris objective and a Nikon DF condenser. An Andor iXonEM + CCD camera (iXon Ultra 897) was employed to record DF images of Ag@AuNRs. The collected images were analyzed with the Image J software. Furthermore, DF scattering spectra were acquired with an Andor spectrophotometer (SHAMROCK 303i, SR-303I-A) and

an Andor CCD camera (Newton DU920P-OE). When recording a spectrum, the scanning stage moved the sample to the desired location was collected by the objective. The scattered light was directed to the entrance of the spectrometer, dispersed by a grating ( $300 \text{ L mm}^{-1}$ ) and detected by the Newton CCD camera. The background was measured at a region without nanoparticles. The collected images were analyzed with the program, Image J. Data analysis on the experimental data was performed by Matlab programs specially designed for this study. The spectra were fitted to a Lorentzian function  $I(\omega) = C_0/[(\omega - \omega_0)^2 + \Gamma^2/4]$  to determine the LSPR linewidth  $\Gamma$  and the resonance frequency  $\omega_0$ .

## **2.4. Raman and SERS measurements**

For SERS sample preparation, a 100- $\mu\text{L}$  aliquot of sample was transferred to a centrifuge tube from the AuNR@Ag (27 nm  $\times$  80 nm) stock solution and centrifuged at 12,000 rpm for 10 min to remove the CTAB surfactant. The rinsed AuNR@Ag sample was resuspended in water, and the probe-molecule solution was added to an appropriate concentration. This colloidal solution was sonicated for a few minutes for adequate dispersion and left at room temperature for approximately 6 h for effective binding. The prepared samples were placed into capillary tubes (wall thickness: 0.25 mm, length: 100 mm). Both ends of the sample capillary tube were sealed to prevent loss of solvent by evaporation. Then, SERS measurements were conducted for the

prepared samples under our lab-built Raman spectroscopic system with a 785-nm diode laser close to the resonant condition of thin AuNRs@Ag (27 nm × 80 nm).

A lab-built confocal Raman spectroscopic system equipped with two different lasers (532 nm and 785 nm) was used in this Raman study. The laser power was set to 60 mW; however, the intensity that actually arrived on the stage was a half of the initial power because of beam losses along the pathlength. A monochromator with a spectral resolution of 0.1 nm was used with a 600-line/mm grating and a slit width of approximately 100 μm. The Raman and SERS spectra were collected using a 40× objective lens with a numerical aperture (NA) of 0.75. An Andor CCD camera (Newton Du9209-OE) was used as a detector, and an Andor spectrometer (SHAMROCK 303i, SR-3031-A) transmitted the electric data as a spectrum. The schematic and real instrument were presented in scheme 2, figure 1.

Bulk Raman spectra of pyridine and its derivatives (4-AP, 4-DMAP) were obtained by confocal Raman spectroscopy with 532-nm laser and 1200 grating (NOST, HEDA). The Raman spectra were collected under the condition of 1-sec exposure time at room temperature using a 100× objective lens with a NA of 0.9. All spectra were obtained and analyzed with the Matlab software.

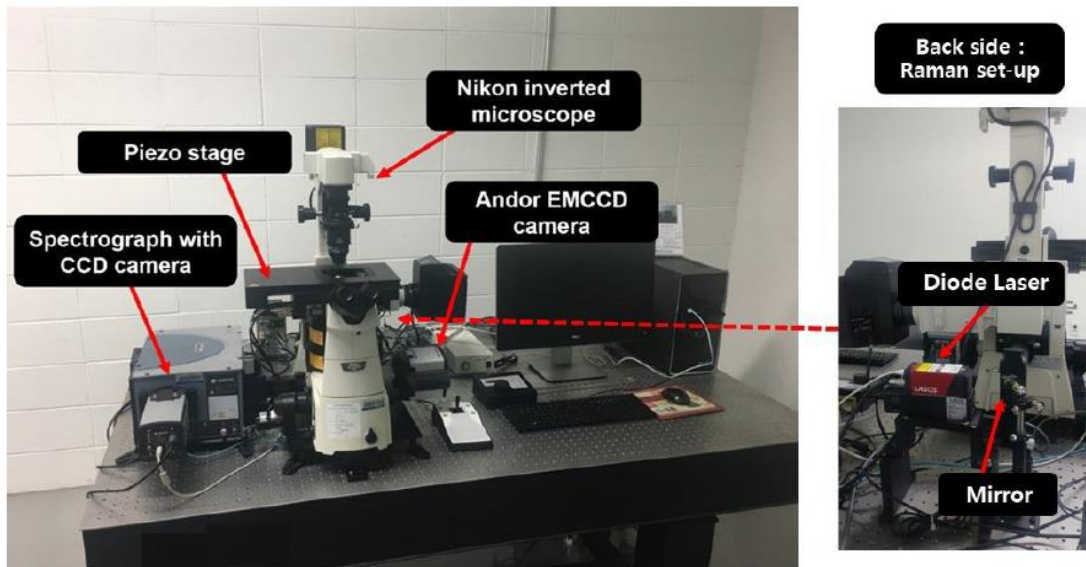
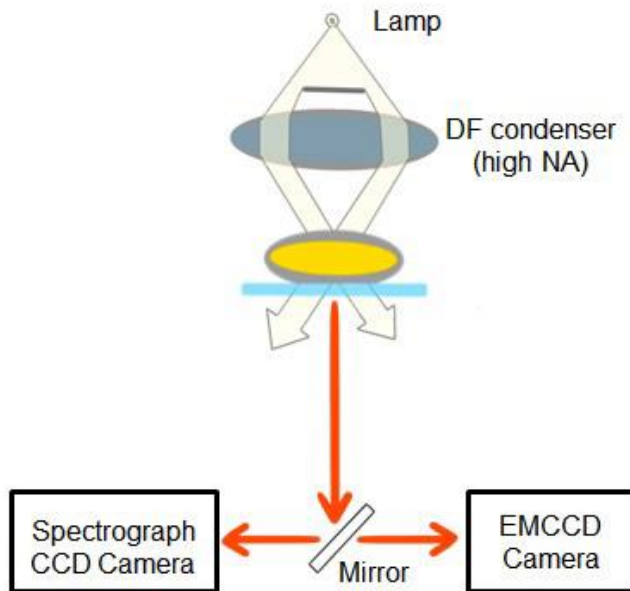
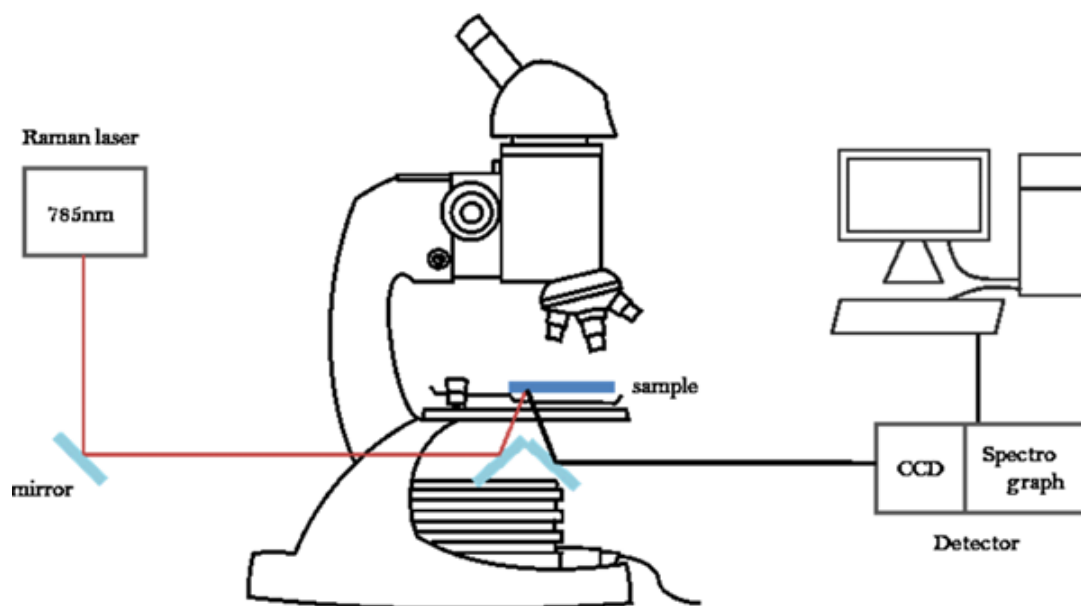


**Figure 1.** A photograph to show the experimental setup for single particle DF spectroscopy and Raman spectroscopy (back-side).



**Scheme 1.** Schematic diagram showing the working principle of scattering-based DF microscopy and spectroscopy.



**Scheme 2.** Experimental setup for surface-enhanced Raman spectroscopy.<sup>70</sup>

### **3. Results and discussion**

#### **3.1. Influence of the Preferred Orientation of Pyridine Derivatives with Donor Substituents on Chemical Interface Damping Induced in Silver-Coated Gold Nanorods with Different Shell Thicknesses**

Figures 2A and B show a schematic of the AuNRs@Ag used in this study, which have two different Ag shell thicknesses and the same size of the AuNR core. Figures 2C and D display TEM images of AuNRs@Ag with a thick Ag shell (thick AuNRs@Ag) and AuNRs@Ag with a thin Ag shell (thin AuNRs@Ag), respectively, in which the difference in the Ag shell thickness between the two samples can be clearly observed. As shown in Figures 2A and B, thick AuNRs@Ag were 92 nm long and 48 nm thick, whereas thin AuNRs@Ag were 80 nm long and 27 nm thick. In addition, as shown in Figure 2, the size of the AuNR core (23 nm × 76 nm on average) was the same for both AuNR@Ag samples. The two different Ag shell thicknesses in AuNRs@Ag were confirmed by the energy dispersive spectroscopy data shown in Figures 3 and 4. Then, we obtained the extinction spectra of both types of AuNRs@Ag using a Varian Cary 300 UV–vis spectrophotometer (Figure 5). The shape-induced characteristic LSPR peaks were observed for AuNRs@Ag dispersed in water. Furthermore, the unique LSPR peaks for Ag were more prominent for AuNRs@Ag with a thick shell in the spectral range between 350 and 450 nm (Figure 5A). However,

the information obtained from ensemble measurements was limited due to the lack of homogeneity; thus, single-particle measurements were required to gain deeper knowledge of detailed optical properties without ensemble averaging. Recently, we reported a single-particle study on the LSPR linewidth broadening in single AuNRs induced by pyridine molecules through Au–nitrogen interaction.<sup>51</sup> However, the effect on CID of using pyridine derivatives with nitrogen and different substituents in AuNRs@Ag remains unknown. Furthermore, to the best of our knowledge, the effect of Ag shell thickness on the CID in AuNRs@Ag has not been investigated yet. Thus, to address these questions, we carried out single-particle DF measurements on AuNRs@Ag having pyridine derivatives with donor substituents at the para position as adsorbates. A photograph of the experimental arrangement for DF scattering studies is shown in Figure 1. Scheme 1 displays a schematic depicting the working principle of DF microscopy; only scattered light from the sample is collected by the objective lens.

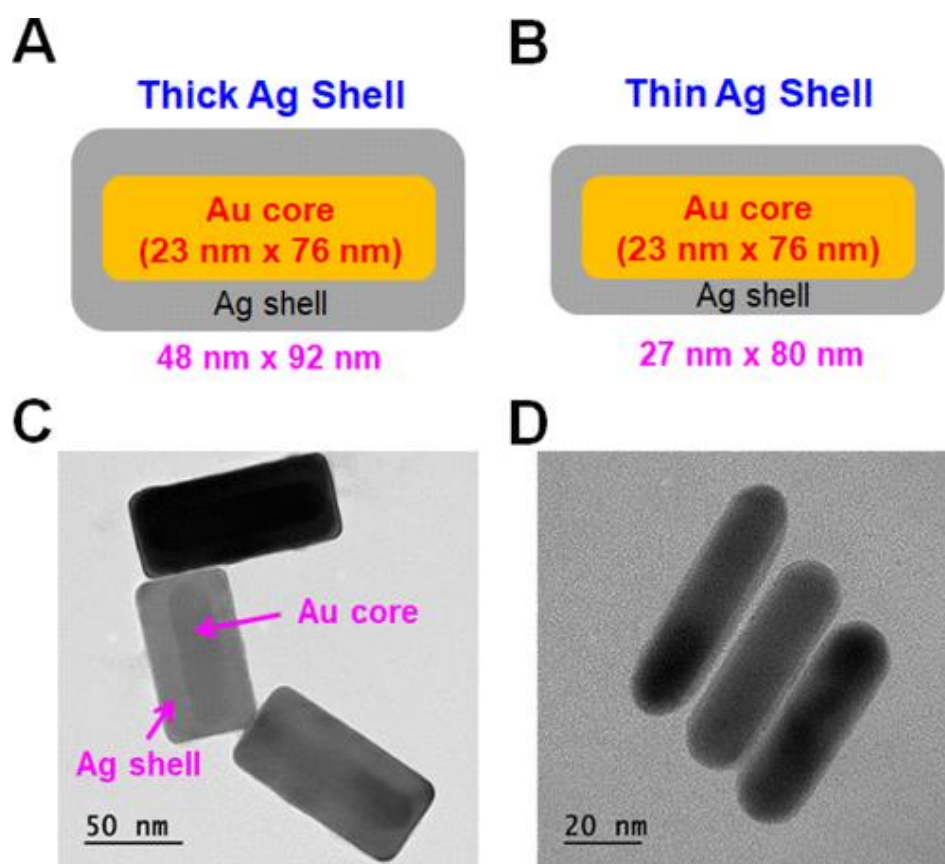
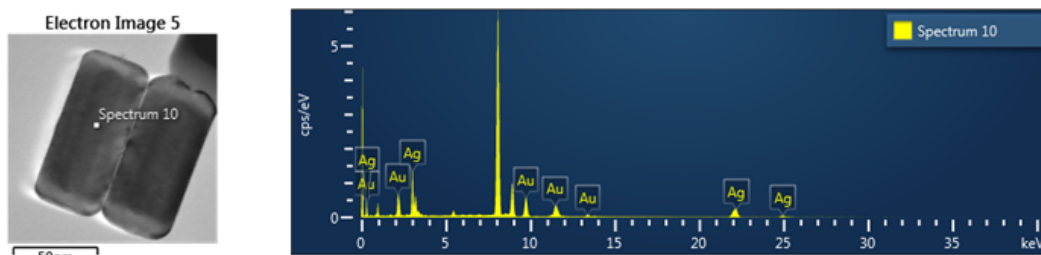
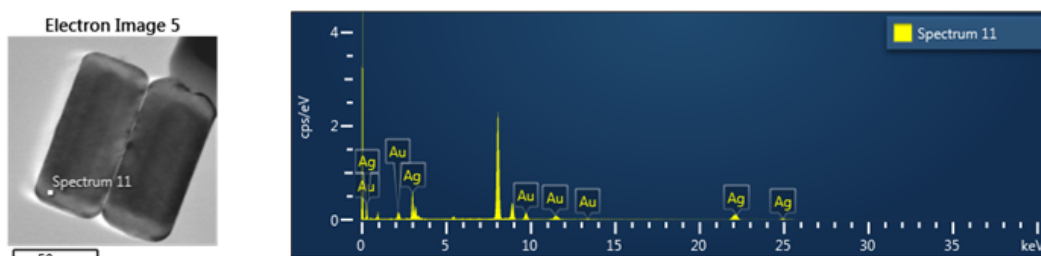


**Figure 2.** (A, B) Schematic diagram showing the dimensions of AuNRs@Ag with two different Ag shell thicknesses. (C, D) TEM images of (C) thick AuNRs@Ag and (D) thin AuNRs@Ag. The Au core and Ag shell are clearly observed in the TEM images.

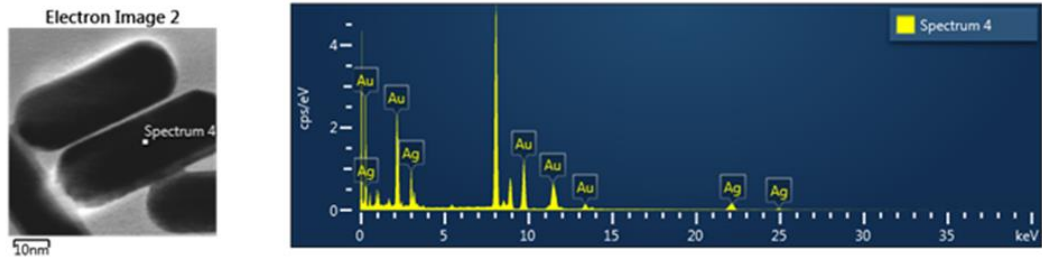


Element	Line Type	k Factor	k Factor type	Absorption Correction	Wt%	Wt% Sigma	Atomic %
Ag	K series	10.456		1.00	67.21	0.60	78.91
Au	L series	2.231		1.00	32.79	0.60	21.09
Total:					100.00		100.00

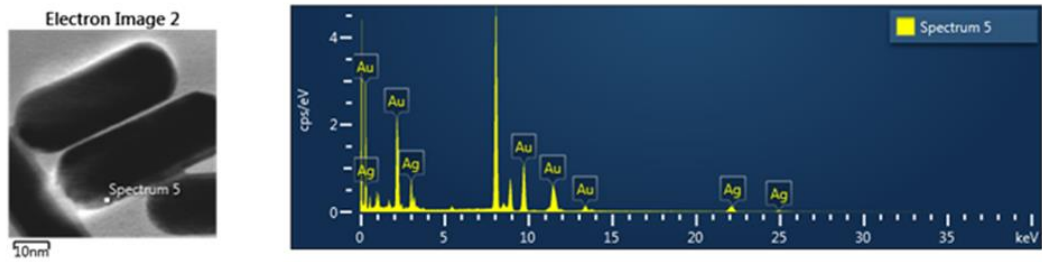


Element	Line Type	k Factor	k Factor type	Absorption Correction	Wt%	Wt% Sigma	Atomic %
Ag	K series	10.456		1.00	79.20	0.46	87.42
Au	L series	2.231		1.00	20.80	0.46	12.58
Total:					100.00		100.00

Figure 3. Energy dispersive spectroscopy data of AuNRs@Ag with thick shell thicknesses.

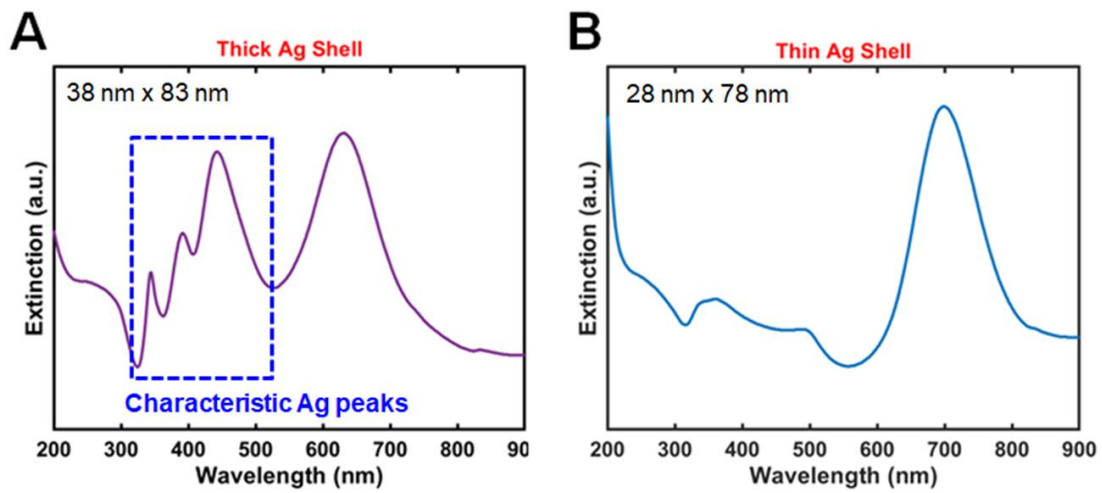


Element	Line Type	k Factor	k Factor type	Absorption Correction	Wt%	Wt% Sigma	Atomic %
Ag	K series	10.456		1.00	38.76	0.84	53.62
Au	L series	2.231		1.00	61.24	0.84	46.38
Total:					100.00		100.00



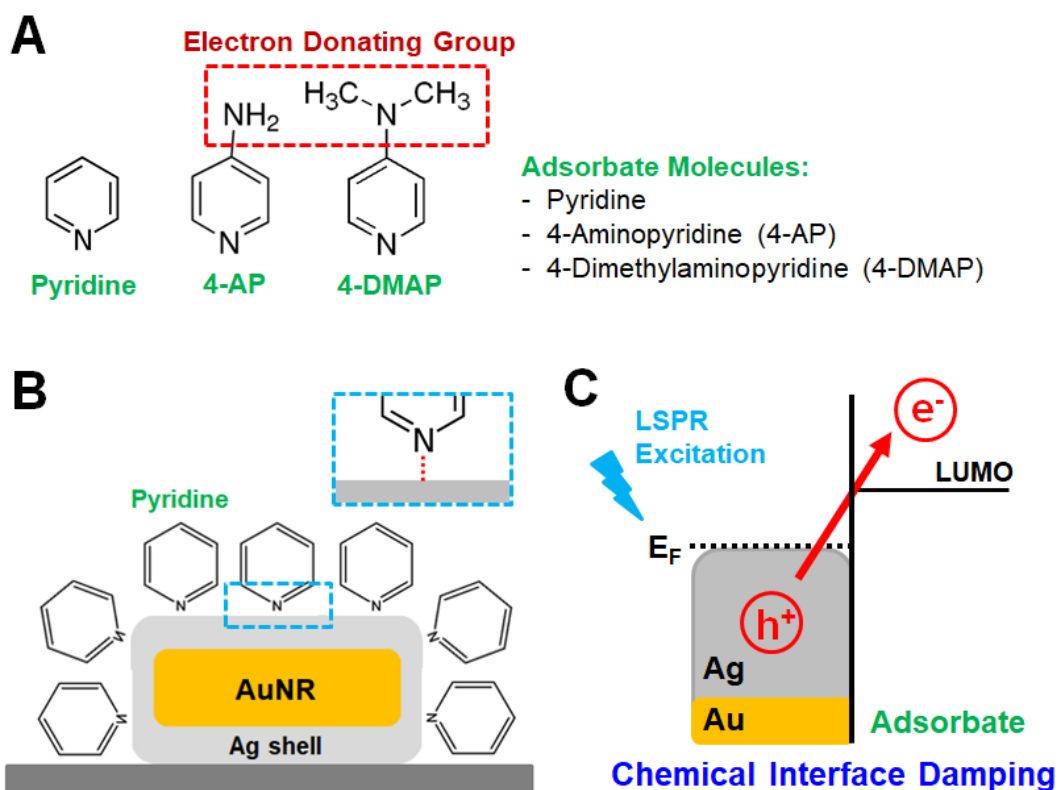
Element	Line Type	k Factor	k Factor type	Absorption Correction	Wt%	Wt% Sigma	Atomic %
Ag	K series	10.456		1.00	35.40	0.87	50.02
Au	L series	2.231		1.00	64.60	0.87	49.98
Total:					100.00		100.00

Figure 4. Energy dispersive spectroscopy data of AuNRs@Ag with thin shell thicknesses.



**Figure 5. (A, B)** UV-Vis extinction spectra of (A) thick AuNRs@Ag in water and (B) thin AuNRs@Ag dispersed in water.

We selected pyridine and pyridine derivatives containing EDGs for two reasons (Figure 6A): first, pyridine molecules having nitrogen substituents have been demonstrated to be effectively adsorbed on metal (Au, Ag) surfaces through the nitrogen lone pair (chemisorption, Figure 6B),<sup>71-74</sup> which allowed us to focus on the effect of the Ag shell thickness on CID induced by pyridine and pyridine derivatives with donor substituents. Second, a recent study revealed that the preferred orientation of pyridine adsorbates on Au changed from perpendicular for pyridine to parallel for pyridine derivatives bearing donor substituents at the para position.<sup>73, 75</sup> Thus, we can investigate how their orientation of adsorption on the AuNR@Ag surfaces affects CID using the direct transfer of hot electrons generated in AuNR@Ag to the empty orbitals (LUMOs) of the adsorbates (Figure 6C).<sup>44-48</sup> It should be noted that CID is strongly affected by the surface coverage (or density) of adsorbate molecules.



**Figure 6.** (A) Schematic diagram showing the chemical structure of pyridine, 4-AP, and 4-DMAP used as adsorbates. (B) Schematic diagram showing the adsorption of pyridine on the Ag surface through nitrogen–Ag interaction. (C) Schematic diagram showing the CID mechanism for the transfer of hot electrons generated in AuNRs@Ag to the empty orbitals (LUMOs) of adsorbates.

Figures 3A and B show DF scattering images of single AuNR@Ag with a thick shell (48 nm × 92 nm) and single AuNR@Ag with a thin shell (27 nm × 80 nm), respectively. As can be seen, the single AuNRs@Ag appear as solid bright spots in a dark background. Figures 3C and D show the DF scattering spectra of thick AuNR1@Ag and thin AuNR1@Ag, respectively. The scattering spectrum of single thick AuNR1@Ag exhibited a peak at approximately 1.92 eV, whereas the LSPR peak of single thin AuNR1@Ag was observed at approximately 1.75 eV. The LSPR linewidth (or full width at half maximum, fwhm) was obtained by Lorentzian fitting; as shown in Figures 3C and D, the experimental data for AuNRs@Ag were fitted well by the Lorentzian function.

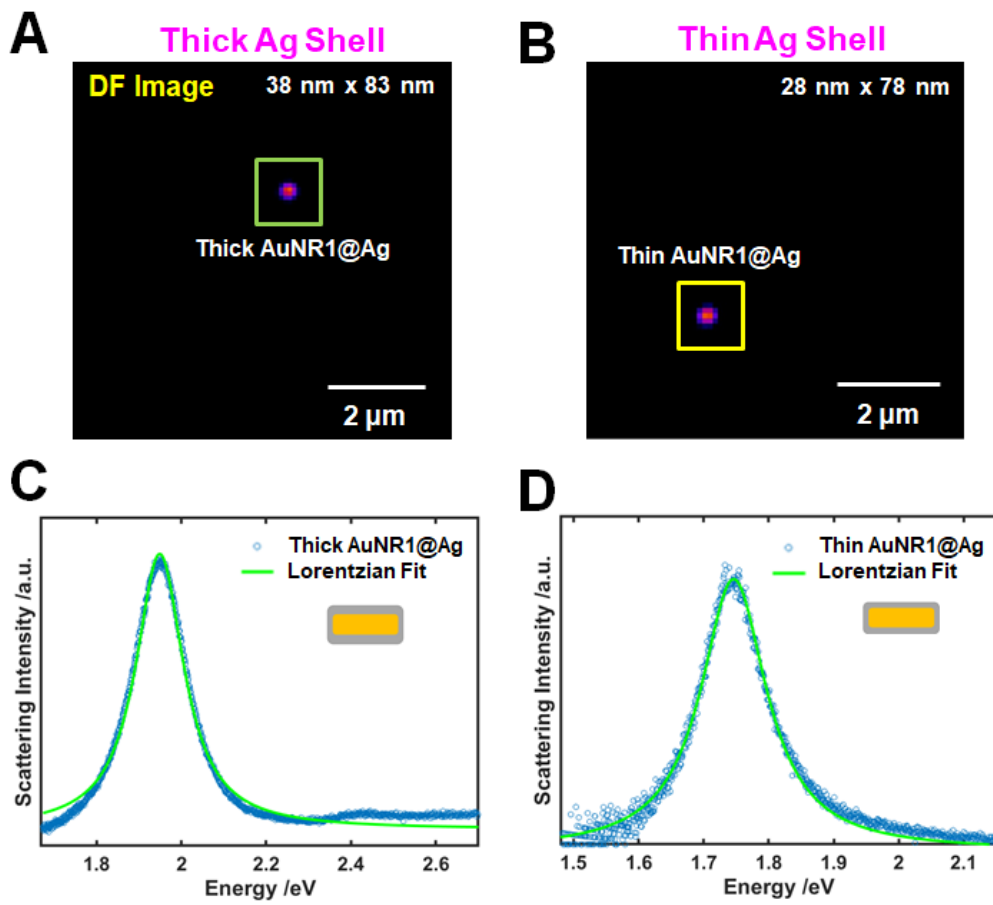


**Figure 7.** (A, B) DF scattering images of (A) thick AuNR@Ag1 and (B) thin AuNR@Ag1. (C, D) Single-particle scattering spectra of (C) thick AuNR@Ag1 and (D) thin AuNR@Ag1. The experimental spectrum (blue curve) is fitted well by the Lorentzian function (green curve).

First, using DF microscopy and spectroscopy, we investigated the broadening of the LSPR linewidth caused by the chemical interactions of pyridine and pyridine derivatives substituted with EDGs in single AuNRs@Ag with two different shell thicknesses. As AuNRs@Ag samples synthesized by wet chemistry have the capping reagent CTAB on the surface, we removed the surfactant layer from the single AuNR@Ag surfaces by oxygen plasma treatment for 10 s in this single-particle study. Subsequently, we obtained the single-particle DF scattering spectra of bare AuNRs@Ag shown in Figures 8A and E, and the corresponding fwhm values were determined by the Lorentzian fitting to be 128 meV for thick AuNRs@Ag and 118 meV for thin AuNRs@Ag. The fwhm value was further determined to be 96.1 meV for bare AuNRs of similar size (25 nm × 73 nm) (Figure 9). Thus, we noticed a much broadened LSPR linewidth for single AuNRs@Ag as compared with that of bare AuNRs without the Ag shell (Figures 8 and 9). Furthermore, single AuNRs@Ag with a thick shell showed more pronounced LSPR linewidth broadening (or plasmon damping) than single AuNRs@Ag with a thin shell (Figures 8A and 8E). Liu and Guyot-Sionnest presented the additional damping primarily ascribed to the interface between Au and Ag.<sup>52</sup> Thus, our results, showing the increase of the fwhm value as the Ag thickness increases, can be attributed to both the increase of the volume plasmon damping and the additional plasmon damping caused by the interface between Au and Ag in single AuNRs@Ag.<sup>52</sup> Then, we introduced pyridine (10 μM) in water to the two differently sized AuNRs@Ag to investigate the CID effect under

DF single-particle microscopy and spectroscopy (Figure 8). Figures 8B and F show that pyridine can induce strong CID through the nitrogen–Ag interaction with a considerable increase in the LSPR linewidth of single AuNRs@Ag. Furthermore, compared with bare AuNRs of similar size, AuNRs@Ag showed stronger CID effect and LSPR linewidth broadening upon the adsorption of pyridine under the same conditions (Figures 8 and 10). This demonstrates that pyridine molecules were effectively bound on the AuNR@Ag surface in the absence of the capping material CTAB, which led to a strong CID effect with a considerably increased LSPR linewidth. In addition, the resonance peak was red-shifted for both thick and thin AuNRs@Ag after the adsorption of pyridine molecules due to the change in the refractive index around the AuNR@Ag (Figure 11).

In addition to pyridine, we further investigated the CID effect using pyridine derivatives with donor substituents in the para position, that is, 4-AP and 4-DMAP, under the same experimental conditions. We introduced the pyridine derivatives (10 $\mu$ M) in water to the two differently sized AuNRs@Ag and obtained the corresponding DF scattering spectra. We found that the homogeneous LSPR linewidth of the AuNRs@Ag decreased for the strong EDG-containing 4-AP and 4-DMAP compared with that for pyridine (Figure 8). Moreover, 4-DMAP showed a more decreased homogeneous LSPR linewidth than 4-AP for both thick and thin AuNRs@Ag.

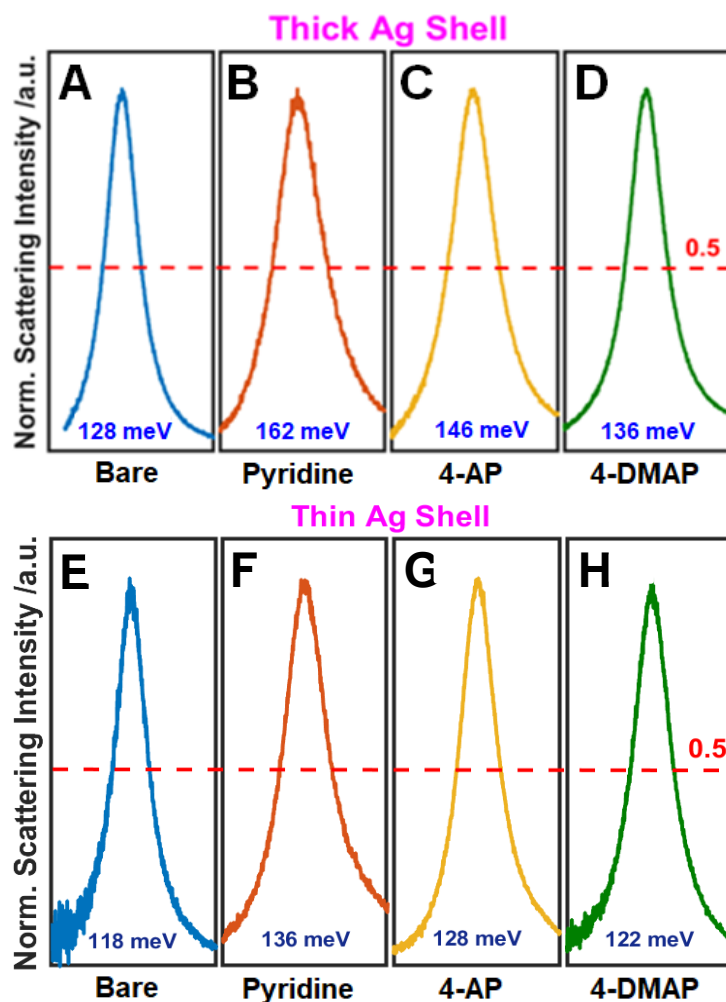
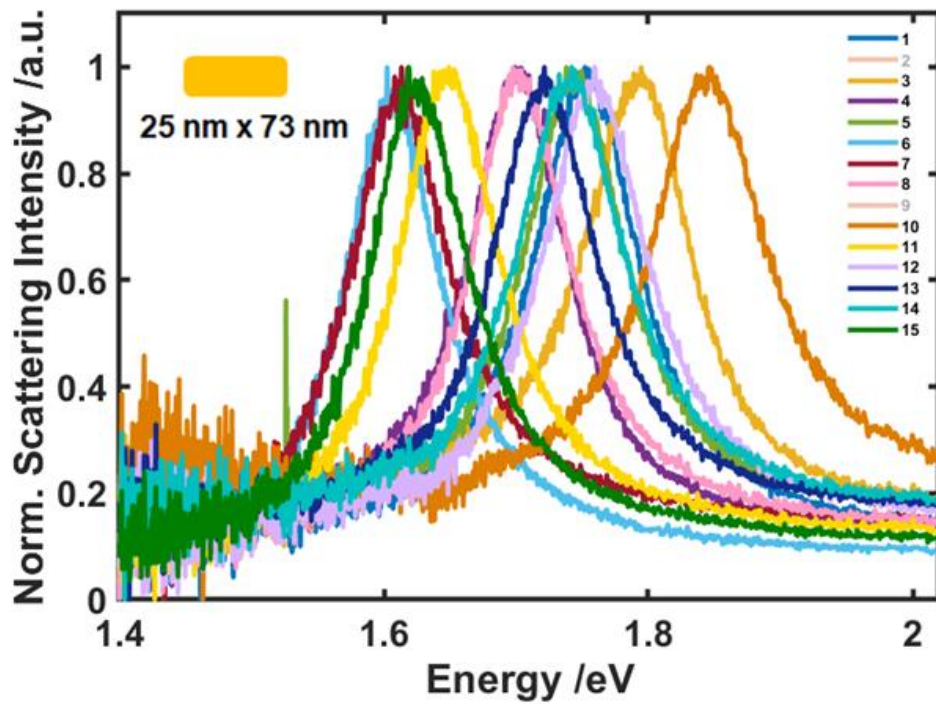
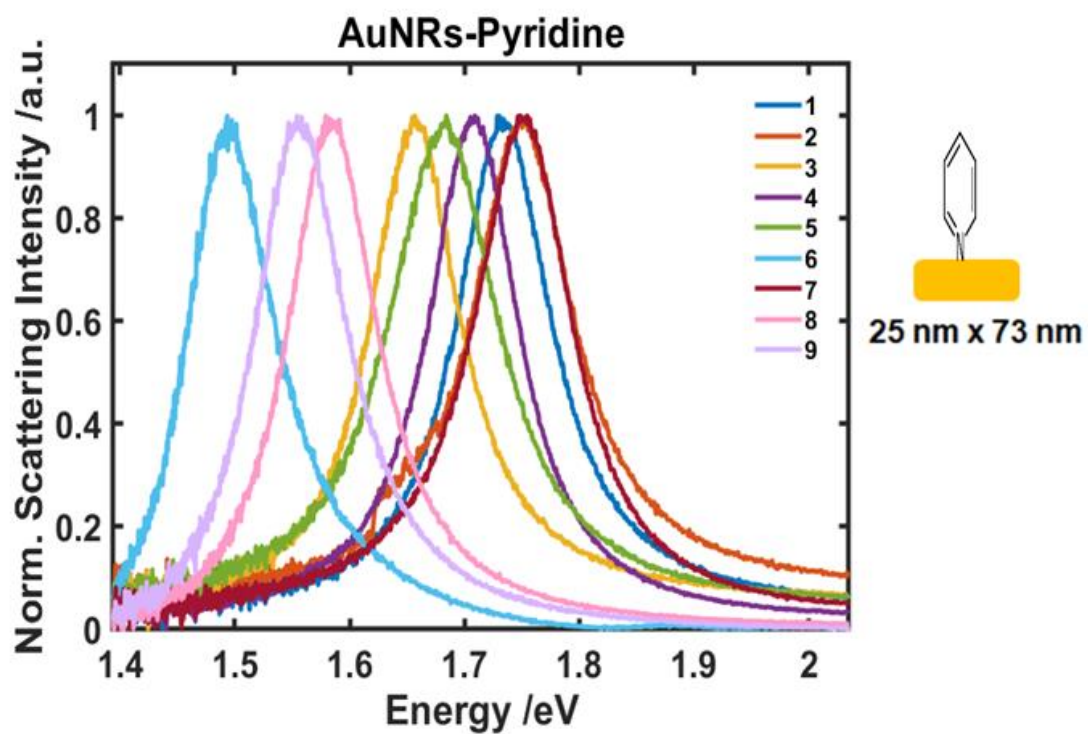


**Figure 8.** (A–D) Single-particle scattering spectra of (A) thick AuNR@Ag upon removal of CTAB (bare), (B) thick AuNR@Ag after the adsorption of pyridine on the surface, (C) thick AuNR@Ag with 4-AP, and (D) thick AuNR@Ag with 4-DMAP. (E–H) Single-particle scattering spectra of (E) thin AuNR@Ag upon removal of CTAB (bare), (F) thin AuNR@Ag after the adsorption of pyridine on the surface, (G) thin AuNR@Ag with 4-AP, and (H) thin AuNR@Ag with 4-DMAP.



**Ave. LSPR Wavelength: 1.71 eV**  
**Ave. LSPR Linewidth: 96.1 meV**

**Figure 9.** Normalized scattering spectra of single AuNRs (on average, 25 nm × 73 nm) without Ag shell. The average LSPR wavelength and linewidth were determined to be 1.71 eV and 96.1 meV, respectively.



**Ave. LSPR Wavelength: 1.62 eV**  
**Ave. LSPR Linewidth: 109.28 meV**

**Figure 10.** Normalized scattering spectra of single AuNRs (on average, 25 nm × 73 nm) upon adsorption of pyridine. The average LSPR wavelength and linewidth were determined to be 1.62 eV and 109.3 meV, respectively.

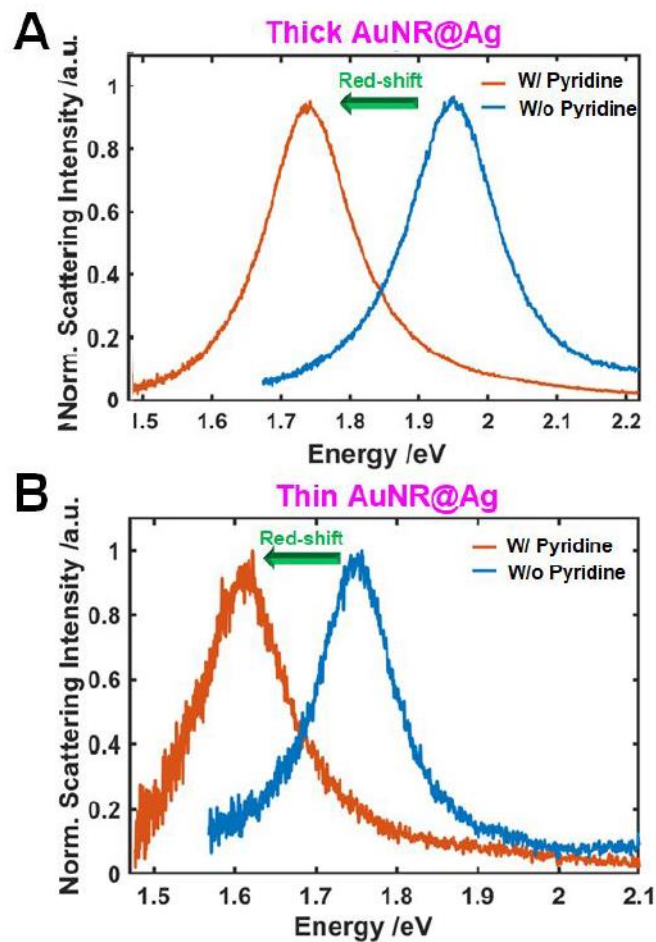


**Figure 11.** (A) Change in the scattering spectrum of thick AuNR@Ag after the adsorption of pyridine molecules. (B) Change in the scattering spectrum of thin AuNR@Ag after the adsorption of pyridine molecules. The scattering spectra were red-shifted for both thick AuNR@Ag and thin AuNR@Ag after the adsorption of pyridine molecules on the particle surface.

To gain a deeper understanding on the CID effect induced by pyridine and the pyridine derivatives, 4-AP and 4-DMAP shown in Figure 8, we performed a statistical analysis with more AuNRs@Ag (thick and thin) measured under the same experimental conditions. Figures 12A and B show the comparison of fwhm values obtained for bare AuNRs@Ag, AuNRs@Ag with pyridine, AuNRs@Ag with 4-AP, and AuNRs@Ag with 4-DMAP for both thick AuNRs@Ag (A) and thin AuNRs@Ag (B). Figure 12A shows that the LSPR linewidth increased by 32.3% from 124 meV (bare) to 164 meV (pyridine), which is consistent with the results extracted from Figures 8A and B for thick AuNRs@Ag. However, for pyridine derivatives with EDGs, the LSPR linewidth decreased from 164 meV for pyridine to 145 meV (4-AP) and 134 meV (4-DMAP) for thick AuNRs@Ag (Figure 12A). In addition, the same tendency and results were observed for thin AuNRs@Ag with respect to pyridine and pyridine derivatives, as shown in Figure 12B. However, thick AuNRs@Ag showed a more increased LSPR linewidth broadening than thin AuNRs@Ag (Figures 12A and B) for all adsorbate molecules. Liu and Guyot-Sionnest ascribed the additional damping primarily to the interface between Au and Ag.<sup>52</sup> However, our result, showing the strong sensitivity of the LSPR linewidth to the surface adsorbates, can suggest that the scattering may be more an effect of the Ag surface. To the best of our knowledge, this is the first report presenting the occurrence of CID induced by pyridine and pyridine derivatives containing EDGs through the strong nitrogen–Ag interaction, and confirming the effect of Ag shell thickness on CID in AuNRs@Ag.

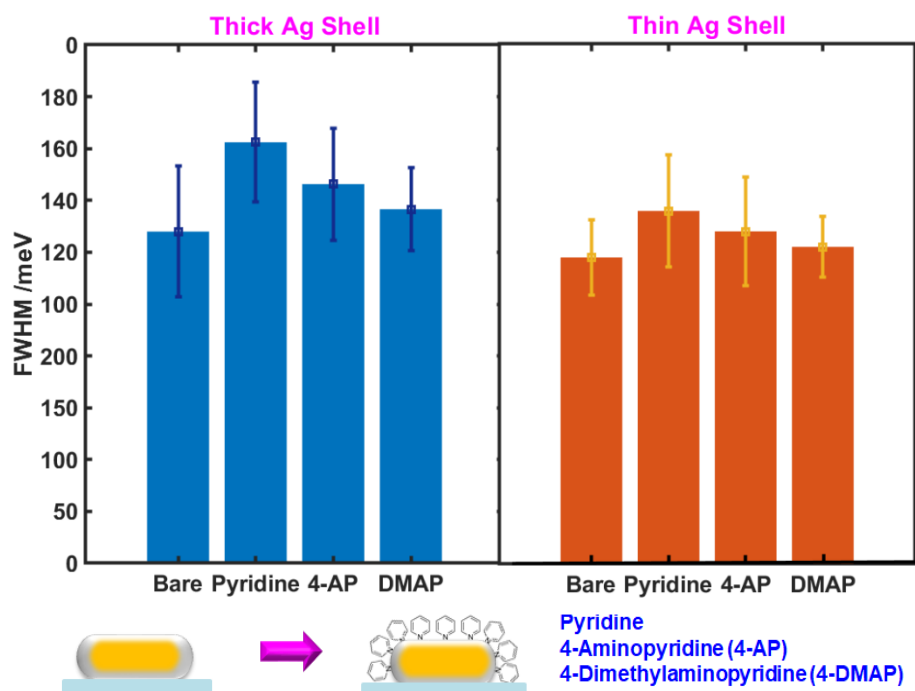


**Figure 12. (A, B)** Comparison of the fwhm values of AuNRs@Ag for bare, pyridine, 4-AP, and 4-DMAP adsorbates under the same experimental conditions. The error bars are based on the determination of the standard deviation measured from ~150 nanoparticles for each sample.

Finally, the results included in Figures 8 and 12 deserve further discussion. The decrease in the fwhm values for the EDG-containing pyridine derivatives (4-AP and 4-DMAP) can be explained from two aspects. First, the decrease in the fwhm values for pyridine derivatives containing EDGs can be ascribed to the interfacial electronic effects on CID. In our previous study, fwhms induced by EDGs were lower than those induced by electron-withdrawing groups.<sup>47</sup> Therefore, the results can be attributed to the impact of the adsorbate on the nature of interfacial nitrogen–Ag bonds. In other words, EDGs can decrease the effectiveness of interfacial nitrogen–Ag bonds on inducing plasmon dephasing during direct interfacial hot-electron transfer or CID.<sup>47</sup> Second, it should be noted that CID is closely related to the surface coverage of adsorbate molecules. Thus, the decrease in the fwhm values can be caused by the difference in the preferred orientation on Ag between pyridine and EDG-containing pyridine derivatives, as shown in Figure 13A. Suzuki et al. showed that pyridine molecules are chemisorbed through nitrogen–Ag bonding with high inclination on the Ag surface.<sup>76</sup> Furthermore, it has been recently shown by quantum chemical calculations that the preferred orientation on Au changes from perpendicular for pyridine to parallel for pyridine derivatives with donor substituents at the para position.<sup>73</sup> Therefore, compared with the perpendicular orientation (or high inclination angle) of pyridine, the preferred orientation of 4-AP and 4-DMAP can be expected to be parallel to the Ag surface, which can lower the surface adsorption coverage (or density) of pyridine derivatives with EDGs at the para position, with the concomitant decrease

in the fwhm values, as shown in Figure 13A. In addition, the fwhm value for 4-DMAP was lower than that of 4-AP, which may be attributed to the steric hindrance effect decreasing the surface coverage (or density). In this study, we confirmed the formation of different orientations for pyridine and pyridine derivatives adsorbed on the Ag surfaces by dynamic light scattering (DLS) measurements (Figure 14).

To shed some light on the preferred orientation of pyridine and EDG-containing pyridine derivatives adsorbed on the Ag surfaces, we further performed Raman scattering and surface-enhanced Raman scattering (SERS) measurements. In the case of chemisorption (e.g., Ag–nitrogen), the adsorbed molecule changes its chemical structure and symmetry because of bond formation with the metal. This stronger adsorption usually introduces frequency shifts of the vibrations of adsorbed molecules in comparison with those of the free molecules.<sup>75, 77</sup> Thus, the presence of frequency shifts in the SERS spectrum in comparison with the bulk Raman spectrum of the same molecule can be used to evaluate the nature of the adsorbate–metal bonding.

In this study, we compared the SERS and Raman spectra of pyridine and pyridine derivatives having EDGs at the para position. Figure 13A displays the schematics showing the preferred orientation of adsorbed pyridine and pyridine derivatives with EDGs on the Ag surface. According to Suzuki and co-workers, pyridine molecules are chemisorbed through nitrogen–Ag bonding with high inclination (or vertical adsorption) on the Ag surface.<sup>76</sup> In this case,  $\sigma$  bonding of the

pyridine nitrogen to the Ag metal causes blue shifts in the SERS spectrum as compared to the bulk Raman spectrum.<sup>78</sup> On the other hand, Mollenhauer et al. reported that 4-AP and 4-DMAP can be adsorbed onto the metal surfaces with the pyridine ring adopting a flat geometry (parallel adsorption).<sup>73</sup> In this case, the SERS peaks are red-shifted compared with the bulk Raman peaks due to  $\pi$  bonding between the pyridine ring and the Ag atom.<sup>75, 78</sup> By comparing the bulk Raman and SERS spectrum of pyridine, we confirmed that the Raman peaks at 1008 and 1036  $\text{cm}^{-1}$  that correspond to the ring breathing mode were blue-shifted in comparison with the SERS peaks at 1024 and 1054  $\text{cm}^{-1}$  (Figure 15).<sup>79, 80</sup> This result indicates that the pyridine ring is tilted from a flat geometry, and that the pyridine nitrogen interacts with the Ag surface through a strong  $\sigma$  bonding.<sup>78</sup> In contrast, we observed red shifts in the SERS spectrum compared with the bulk Raman spectrum for both 4-AP and 4-DMAP (Figures 13B and C). For example, the Raman peaks at 996 (4-AP) and 987  $\text{cm}^{-1}$  (4-DMAP) that correspond to the ring breathing mode were red-shifted compared with the SERS peaks at 862  $\text{cm}^{-1}$  (4-AP) and 779  $\text{cm}^{-1}$  (4-DMAP) due to  $\pi$  bonding between the pyridine ring and the Ag atom.<sup>75, 81</sup> Thus, the result suggests that the pyridine ring is lying flat on the Ag surface through  $\pi$  bonding.<sup>75, 78</sup> In addition,  $\sigma$  bonding between the nitrogen in the amine group and the Ag surface may also have an effect on the formation of the flat geometry, as depicted in Figure 13A. Therefore, we experimentally proved the preferred orientation of pyridine and EDG-containing pyridine derivatives chemisorbed onto the Ag surfaces. Moreover, this study provides deeper

understanding of the effects of pyridine derivatives with donor substituents and the Ag shell thickness on CID in single AuNRs@Ag.

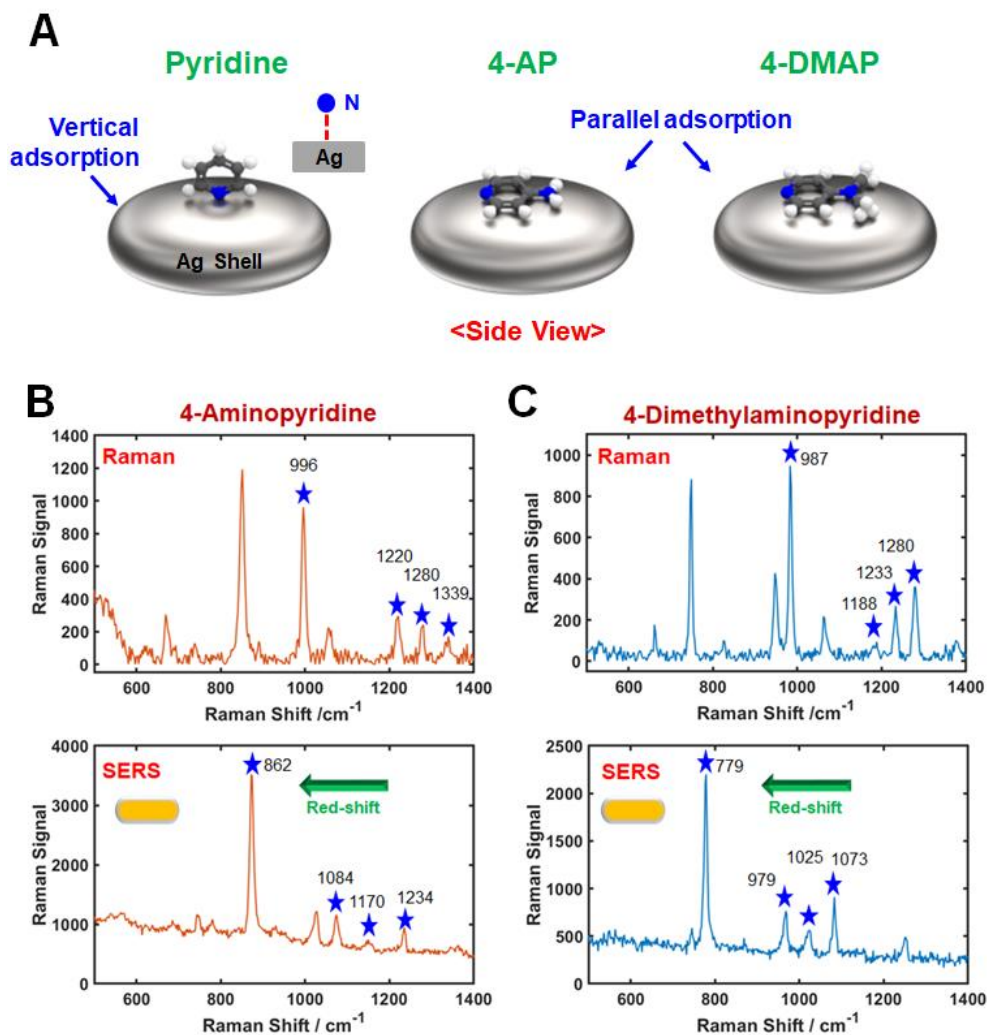


**Figure 13.** (A) Schematics showing the preferred orientation of pyridine and pyridine derivatives with EDGs (4-AP and 4-DMAP). The pyridine molecule is adsorbed onto the Ag surface through a strong nitrogen–Ag interaction. (B) Bulk Raman (top) and SERS (bottom) spectra for 4-AP. (C) Bulk Raman (top) and SERS (bottom) spectra for 4-DMAP. In this study, thin AuNRs@Ag were used for SERS measurements at 785 nm.

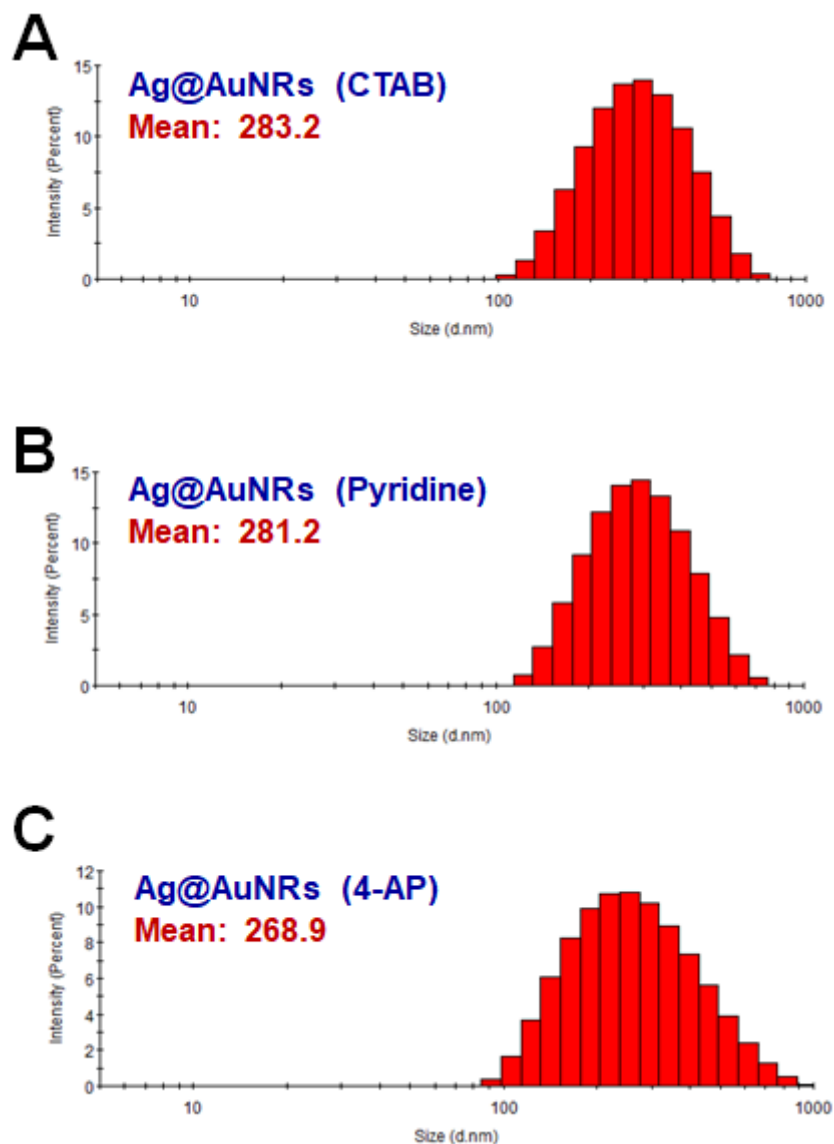


**Figure 14.** (A-C) Dynamic light scattering (DLS) measurements of thick AuNRs@Ag (48 nm×90 nm) with (A) CTAB, (B) pyridine and (C) 4-AP as adsorbates. The change of the particle size of AuNRs@Ag, measured by a DLS measurement. In case of 4-AP, the mean size decreased to 268.9 from 281.2 as compared to that of pyridine.

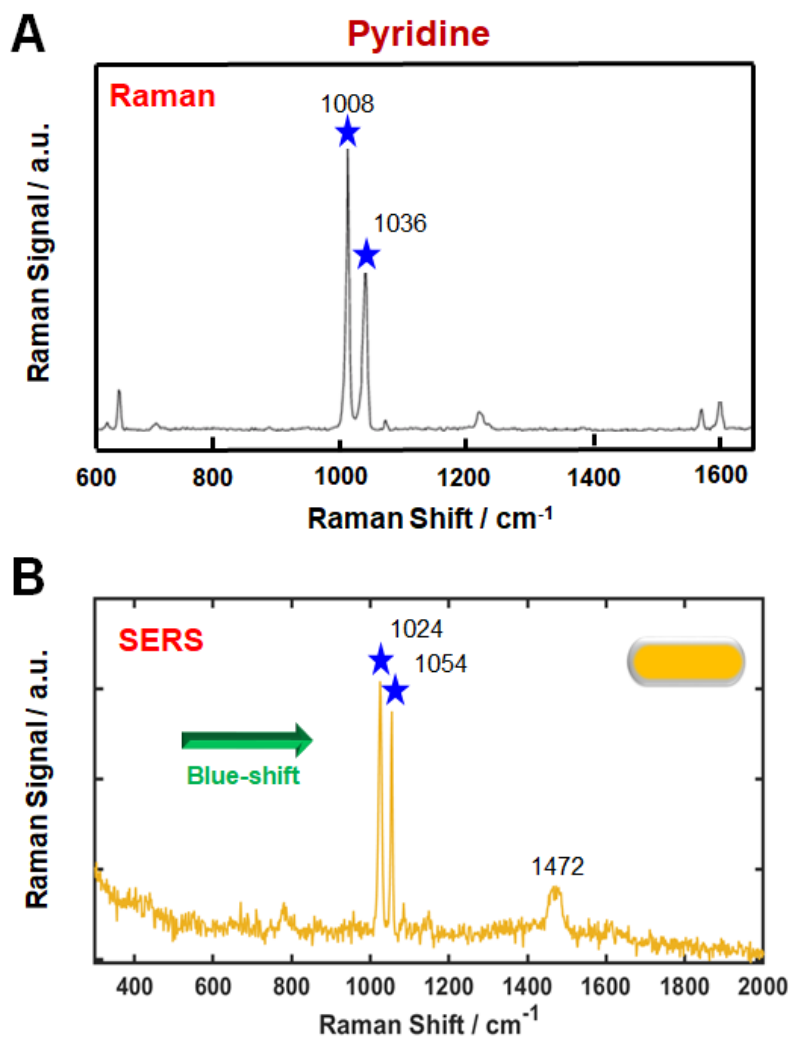


**Figure 15.** (A) Bulk Raman and (B) SERS spectra for pyridine. In this study, thin AuNRs@Ag (28 nm × 78 nm) were used for SERS measurement at 785-nm excitation.

### **3.2. Influence of shell thickness on the refractive index sensitivity of localized surface plasmon resonance inflection points in silver-coated gold nanorods**

This study first attempted to elucidate the scattering properties of single Ag@AuNRs under conventional dark-field (DF) microscopy and spectroscopy.<sup>82</sup> The experimental setup for single particle DF microscopy and spectroscopy is shown in Figure 1. The sample was obtained by drop casting the Ag@AuNRs in water onto a pre-cleaned glass substrate for DF scattering measurements. Subsequently, the prepared samples were illuminated with a tungsten lamp (white light) focused by an oil-immersion condenser with high numerical aperture (NA) and only the light rays that was scattered from the sample was gathered by the objective lens as depicted in Scheme 1. The DF scattering image of single Ag@AuNRs with thick shell thickness is presented in Figure 16A, and the corresponding single particle scattering spectra of four Ag@AuNRs indicated by a green square in (A) are shown in Figure 16B. As shown in Figure 16B, the scattering spectra of thick Ag@AuNRs embedded in water showed a broad LSPR peak at about 1.98 eV. Moreover, a scattering image of single Ag@AuNRs with thin shell thickness (Figure 16C) was obtained, and single thin Ag@AuNRs measured in water also exhibited a broad LSPR peak at about 1.77 eV (Figure 16D).

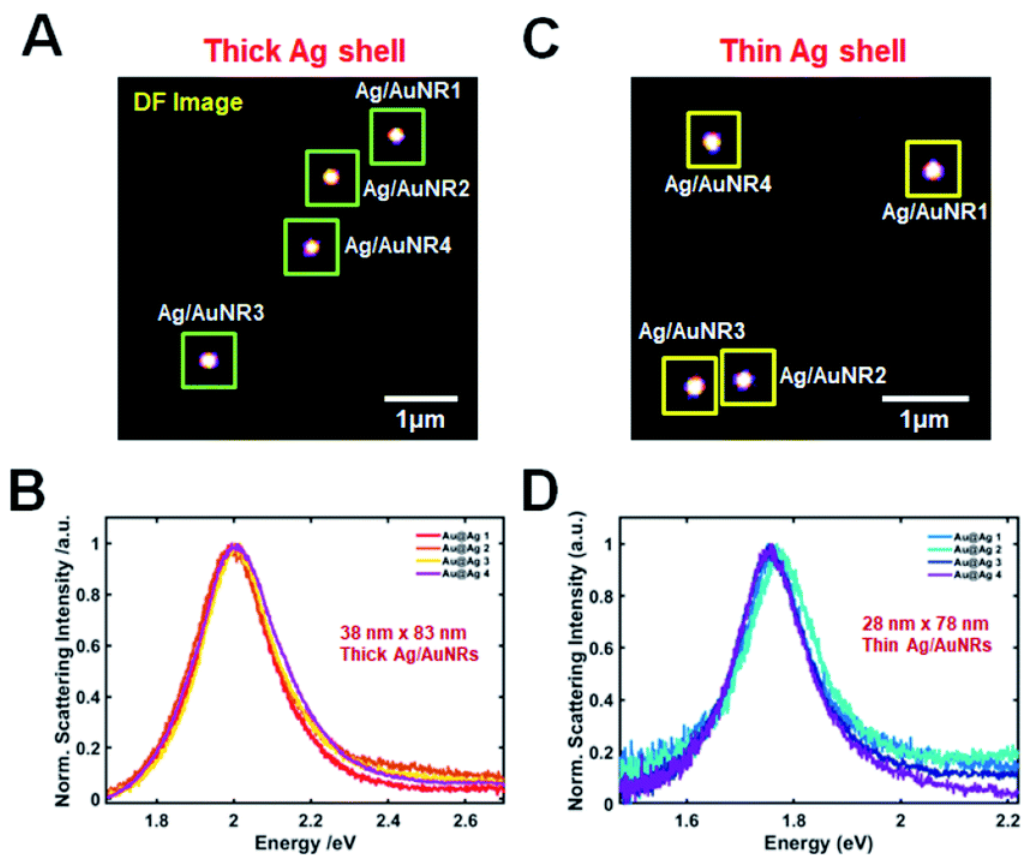


**Figure 16.** (A) Dark-field image of single Ag@AuNRs with thick Ag shell. (B) Corresponding scattering spectra of single Ag@AuNRs with thick Ag shell squared with green in (A). (C) Dark-field image of single Ag@AuNRs with thin Ag shell. (D) Corresponding scattering spectra of single Ag@AuNRs with thin Ag shell squared with yellow in (C).

Subsequently, the influence of changing the RI of the surrounding medium on the LSPR wavelength of Ag@AuNRs having two different shell thickness was investigated. Single particle scattering spectra of Ag@AuNRs were collected in three kinds of RI mediums namely, air, water, and oil. Figures 17A and B show the scattering spectra of single Ag@AuNRs that have different shell thickness, fixed on a slide and surrounded by air, water, and oil. As seen in Figures 17A and B, the LSPR wavelengths of a Ag@AuNR increased with increasing the RI from air to oil, which is in good agreement with the earlier studies.<sup>7, 69</sup> Figure 17C presents the comparison of LSPR frequency shifts with respect to the local RI for thick Ag@AuNR (blue-curve) and thin an Ag@AuNR (red-curve). It was confirmed that Ag@AuNR with thick Ag shell showed increased LSPR frequency shift and RI sensitivity than thin Ag@AuNR (Figures 17C and D). Therefore, the result indicates that single Ag@AuNRs with thick shell thickness yields a higher RI sensitivity in LSPR sensing, which is consistent with the previous results.

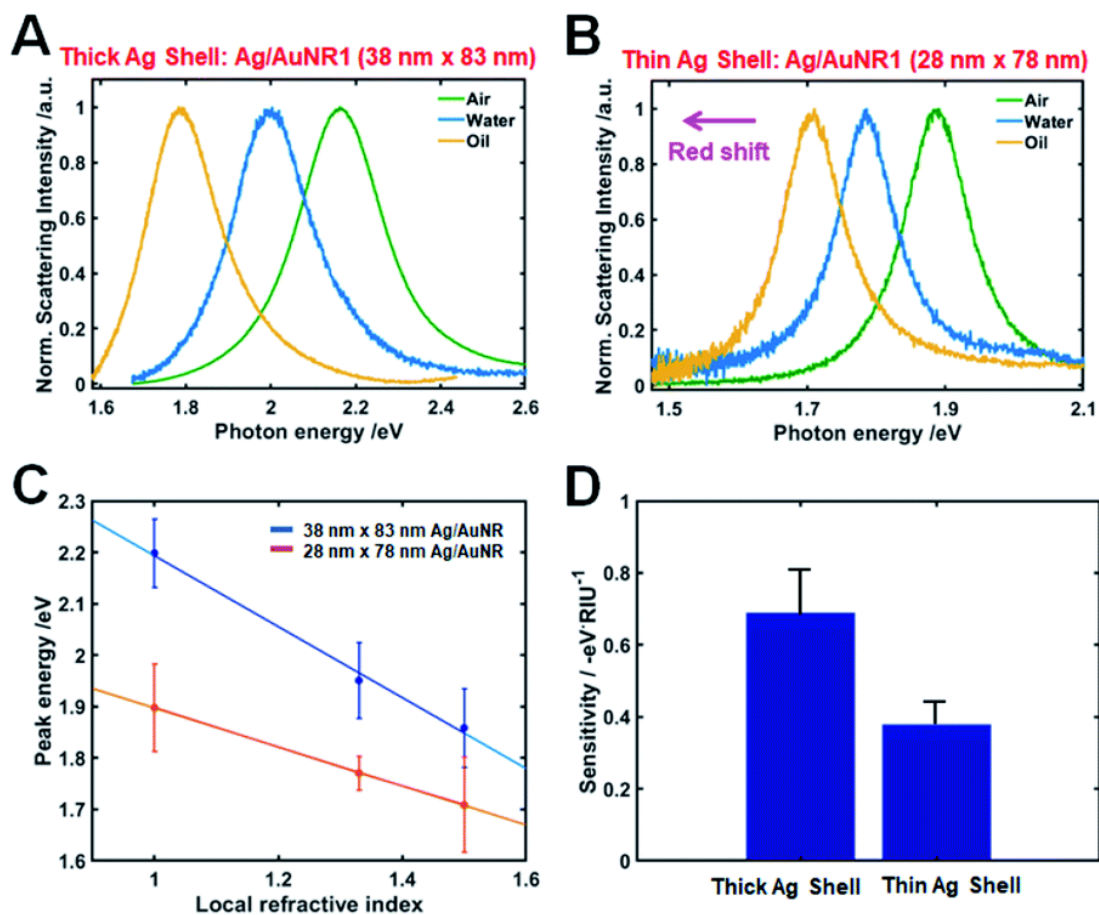


**Figure 17.** (A) Change in the LSPR scattering spectra of single Ag@AuNRs with thick Ag shell in the different local RI media, air, water, oil. (B) Change in the LSPR scattering spectra of single Ag@AuNRs with thin Ag shell in the different local RI media, air, water, oil. (C) LSPR wavelength shifts for thick Ag@AuNRs (blue-curve) and thin Ag@AuNRs (red-curve) as a function of the local RI of medium. (D) Comparison of RI sensitivity at the maximum LSPR wavelength for thick Ag@AuNRs (left) and thin Ag@AuNRs (right).

It has been reported that in single Au bipyramids with sharp tips the LSPR IFs present superior RI sensitivity when compared with the LSPR wavelength maximum peak.<sup>69</sup> Nevertheless, to the best of our knowledge, there have been no studies to report the RI sensitivity of LSPR curvatures (or IFs) in single Ag@AuNRs with variation in Ag shell thickness. We therefore investigated how the shell thickness affects the RI sensitivity at LSPR IFs while considering the first and second derivatives of homogeneous scattering spectra of Ag@AuNRs.<sup>69</sup> The rows 1–3 in Figures 18A–C present the scattering spectra of single Ag@AuNR with thick Ag shell and the respective first and second order derivatives. Unlike the rows, the columns are differentiated by three local RI media used, namely, air, water, and oil. The maxima of LSPR scattering peak in the three mentioned RI environments represented by the legend B occurs at 2.17 eV, 2.04 eV, and 1.82 eV for air, water, and oil, respectively. Additionally, the local minima and maxima of the first order derivatives (shown by A and C respectively) occur at 2.09 eV/2.24 eV, 1.98 eV/2.12 eV and 1.75 eV/1.87 eV for the three different RI media, respectively. It is noticed that markers A and C represent the two LSPR IFs which show a value 0 for the second order derivatives of the LSPR scattering spectra (third row). A match between the local minima/maxima of the first order derivatives and the LSPR IFs is observed at the same points of A and C that occur in the photon energy axis for the three RI media considered. Analogous to the first order derivative, the point B appears to be the critical point of LSPR scattering spectra of Ag@AuNR, which represents null value for the first order

derivatives spectra.

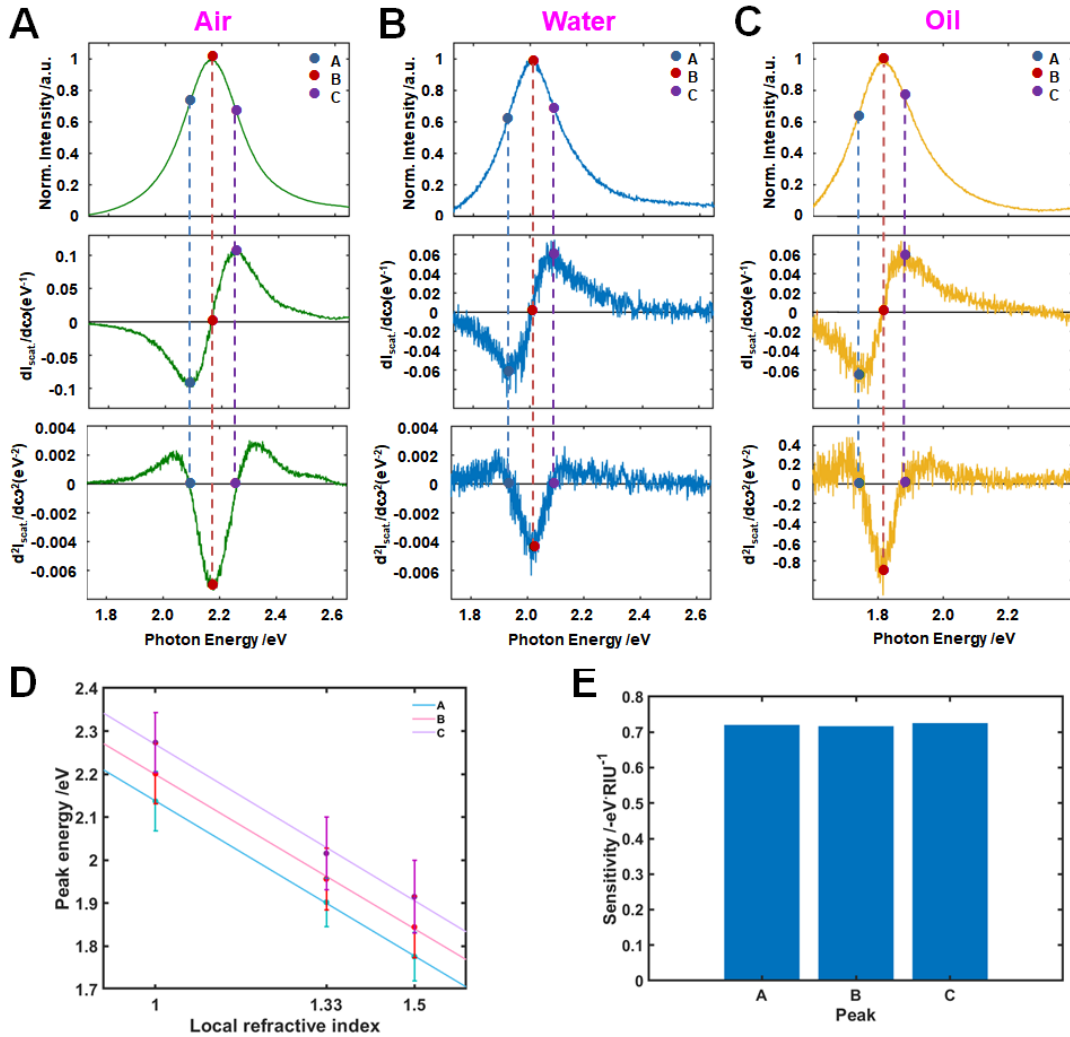


**Figure 18.** Inflection point method for single particle LSPR scattering sensing with Ag@AuNRs with thick Ag shell thickness in the three local refractive indexes (air, water, and oil). (A–C) LSPR scattering efficiencies (first row), LSPR scattering efficiencies first order derivatives (second row), and LSPR scattering efficiencies second order derivatives (third row). (D) Peak energy plotted against the three local RI for A, B, and C. (E) Sensitivity of local RI media on peak shifts A, B and C.

In our previous report, we presented LSPR IFs collected from extinction spectra of gold nanoparticles recorded at the ensemble level.<sup>21</sup> It is evident from Figure 18 that the nature of LSPR scattering spectra of single Ag@AuNRs corresponding to the first and second order derivatives collected in this study are in agreement with our previous report. In addition, it is noticed that the first order derivatives records zero perfectly on the point of symmetry for the three local RI media. This point is represented by the legend B which also marks the LSPR peak maxima. An analysis on the curvature confirmed that both the LSPR scattering curves and second order derivatives are even functions that are symmetric about the intensity axis, whereas, the first order derivatives represent odd functions that are symmetrical about the photon energy axis.

In order to confirm the reproducibility and compatibility of the results shown in Figure 18, we measured and analyzed LSPR scattering spectra of 10 more Ag@AuNRs with thick shell for each local RI environment. The results of these experiments are presented in ESI tables (Tables 1–3), which yielded the LSPR peak maxima (B) to be 2.21 ( $\pm 0.06$ ) eV, 1.96 ( $\pm 0.06$ ) eV and 1.85 ( $\pm 0.01$ ) eV for air, water, and oil RI media, respectively. We then determined the values of LSPR IFs to be 2.15 ( $\pm 0.06$ ) eV (A) and 2.29 ( $\pm 0.06$ ) eV (C), 1.92 ( $\pm 0.04$ ) eV (A) and 2.04 ( $\pm 0.07$ ) eV (C), and 1.78 ( $\pm 0.05$ ) eV (A) and 1.92 ( $\pm 0.05$ ) eV (C), respectively. In the regime relevant to sensing properties, we observed that the peak energies show good approximation linear functions of local RI media.<sup>83</sup> We considered A, B, and C peak energies and

examined their linearity with respect to local air, water, and oil RI media. Figure 18D shows plots of energy peaks A, B, and C against local air, water, and oil RI media with corresponding values equal to 1.00, 1.33, and 1.52, respectively. As demonstrated in Figure 18D, the peak energies at A, B, and C linearized with the local RI media. It should be noted that inflection point C exhibited the highest sensitivity with respect to A and the LSPR peak maxima (B) as shown in Figure 18E.

Thick Ag shell	1	2	3	4	5	6	7	8	9	10	Ave	Std
Inflection A (eV)	2.1145	2.175	2.0987	2.0377	2.2192	2.087	2.2392	2.1761	2.1771	2.1531	<b>2.1477</b>	0.0625
LSPR B (eV)	2.1729	2.2392	2.1624	2.0997	2.2768	2.1635	2.3121	2.2448	2.2336	2.2148	<b>2.212</b>	0.0628
Inflection C (eV)	2.2392	2.3014	2.2358	2.1814	2.3411	2.2493	2.3899	2.3338	2.3014	2.2756	<b>2.285</b>	0.0612

**Table 1.** Inflection points and LSPR peak locations on the curvatures of single Ag@AuNRs with thick Ag shell thickness in refractive index of air

Thick Ag shell	1	2	3	4	5	6	7	8	9	10	Ave	Std
Inflection A (eV)	1.9097	1.9376	1.9759	1.8493	1.9105	1.8373	1.9351	1.9326	1.9376	1.9418	<b>1.917</b>	0.0429
LSPR B (eV)	1.9681	1.9872	2.047	1.8817	1.9604	1.8739	2.0148	2.005	2.0121	1.9952	<b>1.975</b>	0.0566
Inflection C (eV)	2.023	2.0554	2.1175	1.9301	2.0112	1.9219	2.0802	2.062	2.085	2.062	<b>2.035</b>	0.0647

**Table 2.** Inflection points and LSPR peak locations on the curvatures of single Ag@AuNRs with thick shell thickness in refractive index of water

Thick Ag shell	1	2	3	4	5	6	7	8	9	10	Ave	Std
Inflection A (eV)	1.7411	1.7622	1.7547	1.7213	1.7923	1.7391	1.8657	1.7795	1.8175	1.8565	<b>1.783</b>	0.0497
LSPR B (eV)	1.8117	1.8212	1.8161	1.7958	1.8649	1.8059	1.9247	1.8481	1.8955	1.9247	<b>1.851</b>	0.0492
Inflection C (eV)	1.8821	1.89	1.8734	1.8665	1.9397	1.8711	1.9816	1.9363	1.96	1.9859	<b>1.919</b>	0.0473

**Table 3.** Inflection points and LSPR peak locations on the curvatures of single Ag@AuNRs with thick shell thickness in refractive index of oil

To further comprehend the effect of shell thickness on RI sensitivity at the LSPR IFs, Ag@AuNRs with thin shell thickness were measured by scattering-based DF microscopy and spectroscopy. The RI sensitivity of LSPR IFs of thick Ag@AuNRs was then compared with that of thin Ag@AuNRs. Note that both thick Ag@AuNRs and thin Ag@AuNRs have almost same size of AuNR core at the different Ag shell thickness. Therefore, this investigation focuses on influence of the Ag shell thickness of Ag@AuNRs on the RI sensitivity at LSPR IFs at the single particle level.

Similar to the analysis method adopted for thick Ag@AuNRs (Figure 18), we considered the first and second derivatives of our experimental LSPR scattering spectra of Ag@AuNRs with thin shell. The rows 1–3 shown in Figures 19A–C present the scattering spectra of single Ag@AuNRs and the respective first and second order derivatives. The maximum peaks of LSPR scattering curve in the three RI environments air, water, and oil are shown by B. It is noticed that they take the values of 1.91 eV, 1.79 eV, and 1.75 eV. The points of local minima and maxima of the first order derivatives flanking the LSPR peak maxima (B) are represented by A/C, situated at values of 1.87 eV/1.94 eV, 1.76 eV/1.83 eV and 1.71 eV/1.78 eV for air, water, and oil mediums. Consequently, A and C show the two LSPR IFs of thin Ag@AuNRs for which the second order derivatives tend to zero.

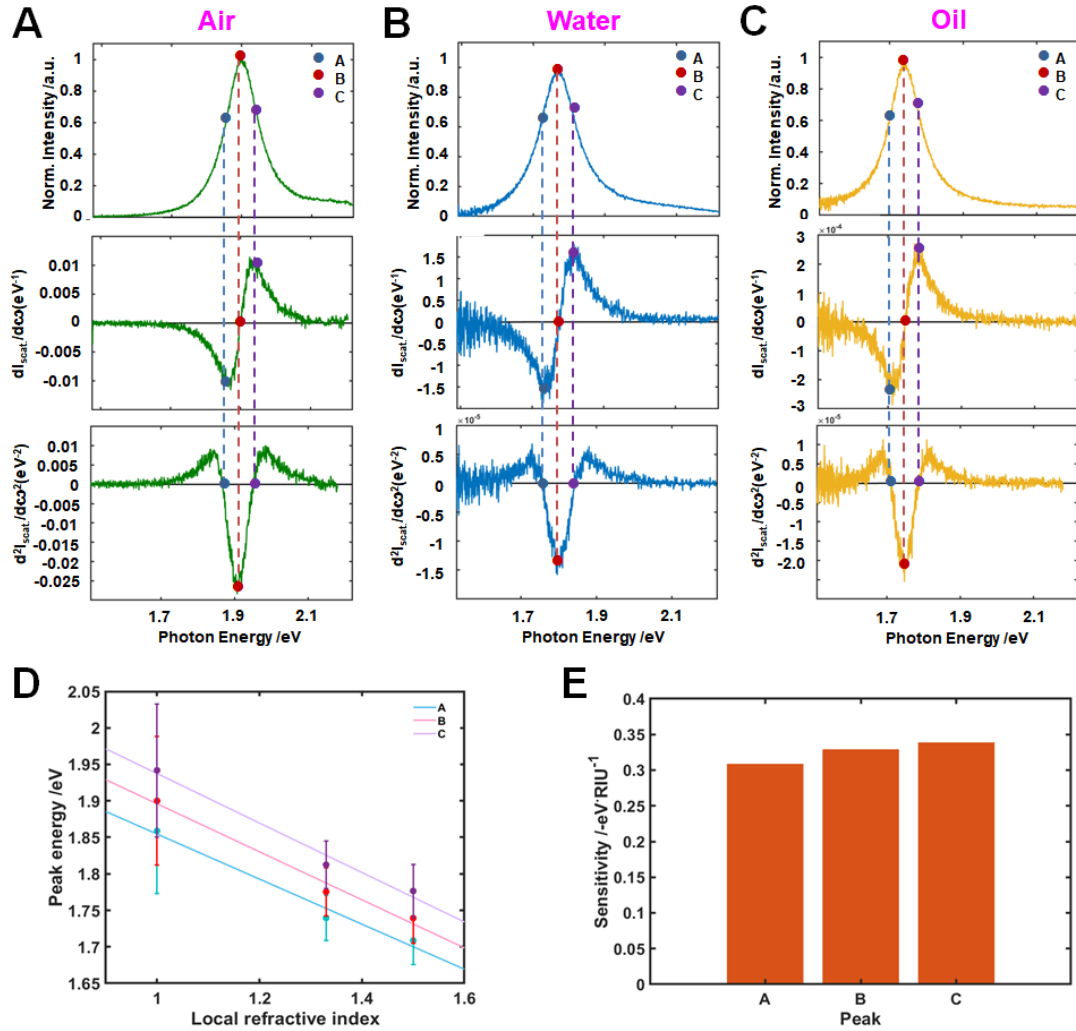


**Figure 19.** Inflection point method for single particle LSPR scattering sensing with Ag@AuNRs with thin Ag shell thickness in the three local refractive indexes (air, water, and oil). (A–C) LSPR scattering efficiencies (first row), LSPR scattering efficiencies first order derivatives (second row), and LSPR scattering efficiencies second order derivatives (third row). (D) Peak energy plotted against the three local RI for A, B, and C. (E) Sensitivity of local RI media on peak shifts A, B and C.

Same results were recorded when we measured the LSPR (B, maximum) scattering spectra of 10 more Ag@AuNRs for each local RI. The values were calculated to be 1.90 ( $\pm 0.09$ ) eV, 1.77 ( $\pm 0.01$ ) eV and 1.74 ( $\pm 0.04$ ) eV for local air, water, and oil RI, respectively (Tables 4–6). Similarly, the LSPR IFs were also computed to be 1.86 ( $\pm 0.09$ ) eV (A) and 1.94 ( $\pm 0.09$ ) eV (C), 1.74 ( $\pm 0.01$ ) eV (A) and 1.81 ( $\pm 0.02$ ) eV (C), and 1.71 ( $\pm 0.03$ ) eV (A) and 1.78 ( $\pm 0.04$ ) eV (C), respectively. We then plotted peak energy A, B, and C as a function of the three selected RI media. As shown in Figure 19D, the peak energies at A, B, and C revealed a linear behavior with the three selected RI media. Similar to the experimental result of thick Ag@AuNRs in Figure 18, it is also notable that inflection point C showed the highest sensitivity with respect to the IF A and the LSPR peaks maxima (B) as clearly presented in Figure 19E. The result is consistent with that of thick Ag@AuNRs in Figure 18. However, it should be noted that the RI sensitivity at IF C of thick Ag@AuNRs in Figure 18D was about 2 times higher than that at IF C of thin Ag@AuNRs in Figure 19E. Therefore, this study found that IF C recorded better RI sensitivity than the LSPR peak maximum for Ag@AuNRs with two different sizes. Furthermore, thick Ag@AuNRs showed higher RI sensitivity than thin Ag@AuNRs at the locations of LSPR peak maximum (B) and LSPR IFs (A, C) (Fig 18E and 19E).

Thin Ag shell	1	2	3	4	5	6	7	8	9	10	Ave	Std
Inflection A (eV)	1.8576	1.9244	1.9452	1.9865	1.7862	1.8692	1.8584	1.7176	1.7855	1.856	<b>1.859</b>	0.0857
LSPR B (eV)	1.8944	1.97	1.9839	2.0314	1.8305	1.9056	1.9129	1.7529	1.8194	1.902	<b>1.9</b>	0.0883
Inflection C (eV)	1.9327	2.0114	2.0205	2.0804	1.8754	1.9385	1.9725	1.7883	1.8569	1.938	<b>1.942</b>	0.0911

**Table 4.** Inflection points and LSPR peak locations on the curvatures of single Ag@AuNRs with thin Ag shell thickness in refractive index of air

Thin Ag shell	1	2	3	4	5	6	7	8	9	10	Ave	Std
Inflection A (eV)	1.7536	1.7347	1.7228	1.7314	1.7414	1.7189	1.7287	1.7597	1.738	1.7215	<b>1.735</b>	0.0135
LSPR B (eV)	1.7912	1.7652	1.7618	1.775	1.775	1.7502	1.7583	1.7933	1.7604	1.7583	<b>1.768</b>	0.0144
Inflection C (eV)	1.8128	1.8005	1.8005	1.8334	1.8297	1.7834	1.8019	1.8267	1.8019	1.7869	<b>1.807</b>	0.0174

**Table 5.** Inflection points and LSPR peak locations on the curvatures of single Ag@AuNRs with thin Ag shell thickness in refractive index of water

Thin Ag shell	1	2	3	4	5	6	7	8	9	10	Ave	Std
Inflection A (eV)	1.7577	1.6571	1.6912	1.7354	1.7228	1.7117	1.6718	1.7515	1.6887	1.6995	<b>1.709</b>	0.0333
LSPR B (eV)	1.799	1.6925	1.7195	1.7625	1.7495	1.7461	1.7001	1.7813	1.7143	1.7287	<b>1.739</b>	0.0348
Inflection C (eV)	1.8402	1.7314	1.7549	1.7983	1.789	1.7827	1.7354	1.8201	1.7481	1.7652	<b>1.776</b>	0.0361

**Table 6.** Inflection points and LSPR peak locations on the curvatures of single Ag@AuNRs with thin Ag shell thickness in refractive index of oil

## 4. Conclusions

In conclusion, we studied the effect of CID according to the adsorption orientation of pyridine derivatives and improving method of RI sensitivity in Au@Ag core shell nanorods. First, we presented DF scattering studies using pyridine and pyridine derivatives containing donor substituents as adsorbates on single AuNRs@Ag having two different shell thicknesses. Pyridine and its derivatives containing EDGs were effectively adsorbed on single AuNRs@Ag after removal of CTAB, and induced a strong homogeneous LSPR linewidth broadening through strong interaction between nitrogen and Ag surfaces. AuNRs@Ag with a thick shell showed a considerably enhanced CID effect compared with that of AuNRs@Ag with a thin shell for all pyridine derivatives. Furthermore, compared to pyridine, pyridine derivatives 4-AP and 4-DMAP caused a decrease in the LSPR linewidth broadening of single AuNRs@Ag under the same experimental conditions. These results can be ascribed to the preferred parallel adsorption of pyridine derivatives with EDGs (which results in lower surface coverage) and to the impact of the adsorbate on the nature of the interfacial Ag–nitrogen bonds for inducing plasmon damping during the CID process. Therefore, this study provides new insights into the effects of pyridine derivatives with donor substituents and the Ag shell thickness on the LSPR linewidth broadening (or CID) in single AuNRs@Ag.

Second, we presented the LSPR sensitivities of single Ag@AuNRs with two

different shell thickness towards changes in the three-different surrounding RI media (air, water, oil). Single Ag@AuNRs with thick shell thickness showed higher RI sensitivity than single Ag@AuNRs with thin shell thickness. Furthermore, higher RI sensitivity was shown at LSPR IF Cs than the variation in the frequency of counterpart LSPR maximum peak for single Au@AuNRs. Therefore, this study provides a deeper insight into the effect of Ag shell thickness on the LSPR RI sensitivity of Ag@AuNRs at LSPR IFs (or curvature). This study further described that homogeneous LSPR IFs in the LSPR scattering spectra of single Ag@AuNRs can be effectively employed for the improvement of sensitivity in LSPR-based RI sensing.

## 5. Reference

1. Hu, M.; Chen, J.; Li, Z.-Y.; Au, L.; Hartland, G. V.; Li, X.; Marquez, M.; Xia, Y., Gold nanostructures: engineering their plasmonic properties for biomedical applications. *Chemical Society Reviews* **2006**, *35* (11), 1084-1094.
2. Nehl, C. L.; Hafner, J. H., Shape-dependent plasmon resonances of gold nanoparticles. *Journal of Materials Chemistry* **2008**, *18* (21), 2415-2419.
3. Nehl, C. L.; Liao, H.; Hafner, J. H., Optical properties of star-shaped gold nanoparticles. *Nano letters* **2006**, *6* (4), 683-688.
4. Sosa, I. O.; Noguez, C.; Barrera, R. G., Optical properties of metal nanoparticles with arbitrary shapes. *The Journal of Physical Chemistry B* **2003**, *107* (26), 6269-6275.
5. Noguez, C., Surface plasmons on metal nanoparticles: the influence of shape and physical environment. *The Journal of Physical Chemistry C* **2007**, *111* (10), 3806-3819.
6. Boyer, D.; Tamarat, P.; Maali, A.; Lounis, B.; Orrit, M., Photothermal imaging of nanometer-sized metal particles among scatterers. *Science* **2002**, *297* (5584), 1160-1163.
7. Chang, W.-S.; Ha, J. W.; Slaughter, L. S.; Link, S., Plasmonic nanorod absorbers as orientation sensors. *Proceedings of the National Academy of Sciences* **2010**, *107* (7), 2781-2786.
8. Zhang, X.-F.; Liu, Z.-G.; Shen, W.; Gurunathan, S., Silver nanoparticles: synthesis, characterization, properties, applications, and therapeutic approaches. *International journal of molecular sciences* **2016**, *17* (9), 1534.
9. Ringe, E.; McMahon, J. M.; Sohn, K.; Cobley, C.; Xia, Y.; Huang, J.; Schatz, G. C.; Marks, L. D.; Van Duyne, R. P., Unraveling the effects of size, composition, and substrate on the localized surface plasmon resonance frequencies of gold and silver nanocubes: a systematic single-particle approach. *The Journal of Physical Chemistry C* **2010**, *114* (29), 12511-12516.
10. Kooij, E. S.; Ahmed, W.; Hellenthal, C.; Zandvliet, H. J.; Poelsema, B., From nanorods to nanostars: Tuning the optical properties of gold nanoparticles. *Colloids and Surfaces A: Physicochemical and Engineering Aspects* **2012**, *413*, 231-238.
11. Anker, J. N.; Hall, W. P.; Lyandres, O.; Shah, N. C.; Zhao, J.; Van Duyne, R. P., Biosensing with plasmonic nanosensors. In *Nanoscience and Technology: A Collection of Reviews from Nature Journals*, World Scientific: 2010; pp 308-319.

12. Loiseau, A.; Asila, V.; Boitel-Aullen, G.; Lam, M.; Salmain, M.; Boujday, S., Silver-based plasmonic nanoparticles for and their use in biosensing. *Biosensors* **2019**, *9* (2), 78.
13. Loiseau, A.; Zhang, L.; Hu, D.; Salmain, M.; Mazouzi, Y.; Flack, R.; Liedberg, B.; Boujday, S., Core–Shell Gold/Silver Nanoparticles for Localized Surface Plasmon Resonance-Based Naked-Eye Toxin Biosensing. *ACS Applied Materials & Interfaces* **2019**, *11* (50), 46462-46471.
14. Chen, A.; Chatterjee, S., Nanomaterials based electrochemical sensors for biomedical applications. *Chemical Society Reviews* **2013**, *42* (12), 5425-5438.
15. Mayer, K. M.; Hafner, J. H., Localized surface plasmon resonance sensors. *Chemical reviews* **2011**, *111* (6), 3828-3857.
16. Boisselier, E.; Astruc, D., Gold nanoparticles in nanomedicine: preparations, imaging, diagnostics, therapies and toxicity. *Chemical society reviews* **2009**, *38* (6), 1759-1782.
17. Dreaden, E. C.; Alkilany, A. M.; Huang, X.; Murphy, C. J.; El-Sayed, M. A., The golden age: gold nanoparticles for biomedicine. *Chemical Society Reviews* **2012**, *41* (7), 2740-2779.
18. Zhou, M.; Li, M.; Hou, C.; Li, Z.; Wang, Y.; Xiang, K.; Guo, X., Pt nanocrystallines/TiO<sub>2</sub> with thickness-controlled carbon layers: Preparation and activities in CO oxidation. *Chinese Chemical Letters* **2018**, *29* (6), 787-790.
19. Zhou, M.; Lin, M.; Chen, L.; Wang, Y.; Guo, X.; Peng, L.; Guo, X.; Ding, W., Thickness-dependent SERS activities of gold nanosheets controllably synthesized via photochemical reduction in lamellar liquid crystals. *Chemical Communications* **2015**, *51* (24), 5116-5119.
20. Zhou, M.; Lin, M.; Wang, Y.; Guo, X.; Guo, X.; Peng, L.; Ding, W., Organic-free synthesis of ultrathin gold nanowires as effective SERS substrates. *Chemical Communications* **2015**, *51* (59), 11841-11843.
21. Guo, L.; Jackman, J. A.; Yang, H.-H.; Chen, P.; Cho, N.-J.; Kim, D.-H., Strategies for enhancing the sensitivity of plasmonic nanosensors. *Nano Today* **2015**, *10* (2), 213-239.
22. Rycenga, M.; Cobley, C. M.; Zeng, J.; Li, W.; Moran, C. H.; Zhang, Q.; Qin, D.; Xia, Y., Controlling the synthesis and assembly of silver nanostructures for plasmonic applications. *Chemical reviews* **2011**, *111* (6), 3669-3712.
23. Sepúlveda, B.; Angelomé, P. C.; Lechuga, L. M.; Liz-Marzán, L. M., LSPR-based nanobiosensors. *nano today* **2009**, *4* (3), 244-251.
24. Jakab, A.; Rosman, C.; Khalavka, Y.; Becker, J.; Trügler, A.; Hohenester, U.;

- Sonnichsen, C., Highly sensitive plasmonic silver nanorods. *ACS nano* **2011**, *5* (9), 6880-6885.
25. Kim, M.; Lin, M.; Son, J.; Xu, H.; Nam, J. M., Hot-Electron-Mediated Photochemical Reactions: Principles, Recent Advances, and Challenges. *Advanced Optical Materials* **2017**, *5* (15), 1700004.
26. Zhang, Y.; He, S.; Guo, W.; Hu, Y.; Huang, J.; Mulcahy, J. R.; Wei, W. D., Surface-plasmon-driven hot electron photochemistry. *Chemical reviews* **2017**, *118* (6), 2927-2954.
27. Pelton, M.; Liu, M.; Park, S.; Scherer, N. F.; Guyot-Sionnest, P., Ultrafast resonant optical scattering from single gold nanorods: Large nonlinearities and plasmon saturation. *Physical Review B* **2006**, *73* (15), 155419.
28. Hoggard, A.; Wang, L.-Y.; Ma, L.; Fang, Y.; You, G.; Olson, J.; Liu, Z.; Chang, W.-S.; Ajayan, P. M.; Link, S., Using the plasmon linewidth to calculate the time and efficiency of electron transfer between gold nanorods and graphene. *ACS nano* **2013**, *7* (12), 11209-11217.
29. Novo, C.; Gomez, D.; Perez-Juste, J.; Zhang, Z.; Petrova, H.; Reismann, M.; Mulvaney, P.; Hartland, G. V., Contributions from radiation damping and surface scattering to the linewidth of the longitudinal plasmon band of gold nanorods: a single particle study. *Physical Chemistry Chemical Physics* **2006**, *8* (30), 3540-3546.
30. Sonnichsen, C., Drastic reduction of plasmon damping in gold nanorods. *Phys. Rev. Lett.* **2002**, *88*, 077402-1.
31. Olson, J.; Dominguez-Medina, S.; Hoggard, A.; Wang, L.-Y.; Chang, W.-S.; Link, S., Optical characterization of single plasmonic nanoparticles. *Chemical Society Reviews* **2015**, *44* (1), 40-57.
32. Hafner, J. H.; Nehl, C. L.; Goodrich, G. P.; Tam, F.; Halas, N. J., Scattering Spectra of Single Gold Nanoshells. *APS* **2004**, *2004*, S34. 002.
33. Hu, M.; Novo, C.; Funston, A.; Wang, H.; Staleva, H.; Zou, S.; Mulvaney, P.; Xia, Y.; Hartland, G. V., Dark-field microscopy studies of single metal nanoparticles: understanding the factors that influence the linewidth of the localized surface plasmon resonance. *Journal of materials chemistry* **2008**, *18* (17), 1949-1960.
34. Hu, M.; Petrova, H.; Sekkinen, A. R.; Chen, J.; McLellan, J. M.; Li, Z.-Y.; Marquez, M.; Li, X.; Xia, Y.; Hartland, G. V., Optical properties of Au–Ag nanoboxes studied by single nanoparticle spectroscopy. *The Journal of Physical Chemistry B* **2006**, *110* (40), 19923-19928.

35. Wang, X.; Zhang, Z.; Hartland, G. V., Electronic Dephasing in Bimetallic Gold–Silver Nanoparticles Examined by Single Particle Spectroscopy. *The Journal of Physical Chemistry B* **2005**, *109* (43), 20324-20330.
36. Foerster, B.; Joplin, A.; Kaefer, K.; Celiksoy, S.; Link, S.; Sönnichsen, C., ACS Nano 2017, *11*, 2886–2893. DOI.
37. Ha, J. W., Chemical interface damping of single gold nanorods with low sensitivity to the medium dielectric constant. *Chemical Physics Letters* **2017**, *676*, 65-69.
38. Ha, J. W.; Sun, W.; Stender, A. S.; Fang, N., Dual-wavelength detection of rotational diffusion of single anisotropic nanocarriers on live cell membranes. *The Journal of Physical Chemistry C* **2012**, *116* (4), 2766-2771.
39. Hu, M.; Chen, J.; Marquez, M.; Xia, Y.; Hartland, G. V., Correlated Rayleigh Scattering Spectroscopy and Scanning Electron Microscopy Studies of Au– Ag Bimetallic Nanoboxes and Nanocages. *The Journal of Physical Chemistry C* **2007**, *111* (34), 12558-12565.
40. Zijlstra, P.; Paulo, P. M.; Yu, K.; Xu, Q. H.; Orrit, M., Chemical Interface Damping in Single Gold Nanorods and Its Near Elimination by Tip-Specific Functionalization. *Angewandte Chemie* **2012**, *124* (33), 8477-8480.
41. Foerster, B.; Spata, V. A.; Carter, E. A.; Sönnichsen, C.; Link, S., Plasmon damping depends on the chemical nature of the nanoparticle interface. *Science advances* **2019**, *5* (3), eaav0704.
42. Kreibig, U., Interface-induced dephasing of Mie plasmon polaritons. *Applied physics B* **2008**, *93* (1), 79-89.
43. Wu, K.; Chen, J.; McBride, J.; Lian, T., Molecular interfaces for plasmonic hot electron photovoltaics. Efficient hot-electron transfer by a plasmon-induced interfacial charge-transfer transition. *Science* **2015**, *349*, 632-635.
44. Brongersma, M. L.; Halas, N. J.; Nordlander, P., Plasmon-induced hot carrier science and technology. *Nature nanotechnology* **2015**, *10* (1), 25-34.
45. Christopher, P.; Moskovits, M., Hot charge carrier transmission from plasmonic nanostructures. *Annual review of physical chemistry* **2017**, *68*, 379-398.
46. Govorov, A. O.; Zhang, H.; Gun'ko, Y. K., Theory of photoinjection of hot plasmonic carriers from metal nanostructures into semiconductors and surface molecules. *The Journal of Physical Chemistry C* **2013**, *117* (32), 16616-16631.
47. Lee, S. Y.; Tsalu, P. V.; Kim, G. W.; Seo, M. J.; Hong, J. W.; Ha, J. W., Tuning chemical interface damping: Interfacial electronic effects of adsorbate molecules and sharp

- tips of single gold bipyramids. *Nano Letters* **2019**, *19* (4), 2568-2574.
48. Moon, S. W.; Ha, J. W., Single-particle correlation study: chemical interface damping induced by biotinylated proteins with sulfur in plasmonic gold nanorods. *Physical Chemistry Chemical Physics* **2019**, *21* (13), 7061-7066.
49. Therrien, A. J.; Kale, M. J.; Yuan, L.; Zhang, C.; Halas, N. J.; Christopher, P., Impact of chemical interface damping on surface plasmon dephasing. *Faraday discussions* **2019**, *214*, 59-72.
50. Moon, S. W.; Tsalu, P. V.; Ha, J. W., Single particle study: size and chemical effects on plasmon damping at the interface between adsorbate and anisotropic gold nanorods. *Physical Chemistry Chemical Physics* **2018**, *20* (34), 22197-22202.
51. Moon, S. W.; Ha, J. W., Influence of the capping material on pyridine-induced chemical interface damping in single gold nanorods. *Analyst* **2019**, *144* (8), 2679-2683.
52. Liu, M.; Guyot-Sionnest, P., Synthesis and optical characterization of Au/Ag core/shell nanorods. *The Journal of Physical Chemistry B* **2004**, *108* (19), 5882-5888.
53. Fleischmann, M.; Hendra, P. J.; McQuillan, A. J., Raman spectra of pyridine adsorbed at a silver electrode. *Chemical physics letters* **1974**, *26* (2), 163-166.
54. Kneipp, K.; Wang, Y.; Kneipp, H.; Perelman, L. T.; Itzkan, I.; Dasari, R. R.; Feld, M. S., Single molecule detection using surface-enhanced Raman scattering (SERS). *Physical review letters* **1997**, *78* (9), 1667.
55. Nie, S.; Emory, S. R., Probing single molecules and single nanoparticles by surface-enhanced Raman scattering. *science* **1997**, *275* (5303), 1102-1106.
56. Radziuk, D.; Moehwald, H., Highly effective hot spots for SERS signatures of live fibroblasts. *Nanoscale* **2014**, *6* (11), 6115-6126.
57. Billmann, J.; Otto, A., Experimental evidence for a local mechanism of surface enhanced Raman scattering. *Applications of Surface Science* **1980**, *6* (3-4), 356-361.
58. Bloxham, S.; Eicher-Lorka, O.; Jakubėnas, R.; Niaura, G., Adsorption of Cysteamine at Copper Electrodes as Studied by Surface-Enhanced Raman Spectroscopy. *Spectroscopy letters* **2003**, *36* (3), 211-226.
59. Schatz, G. C.; Young, M. A.; Van Duyne, R. P., Electromagnetic mechanism of SERS. In *Surface-enhanced Raman scattering*, Springer: 2006; pp 19-45.
60. Yamada, H.; Nagata, H.; Toba, K.; Nakao, Y., Charge-transfer band and SERS mechanism for the pyridine-Ag system. *Surface science* **1987**, *182* (1-2), 269-286.
61. Kleinman, S. L.; Frontiera, R. R.; Henry, A.-I.; Dieringer, J. A.; Van Duyne, R. P., Creating, characterizing, and controlling chemistry with SERS hot spots. *Physical Chemistry*

*Chemical Physics* **2013**, *15* (1), 21-36.

62. Campion, A.; Kambhampati, P., Surface-enhanced Raman scattering. *Chemical society reviews* **1998**, *27* (4), 241-250.

63. Lombardi, J. R.; Birke, R. L.; Lu, T.; Xu, J., Charge-transfer theory of surface enhanced Raman spectroscopy: Herzberg–Teller contributions. *The Journal of chemical physics* **1986**, *84* (8), 4174-4180.

64. Chen, P.; Liedberg, B., Curvature of the localized surface plasmon resonance peak. *Analytical chemistry* **2014**, *86* (15), 7399-7405.

65. Derkachova, A.; Kolwas, K.; Demchenko, I., Dielectric function for gold in plasmonics applications: size dependence of plasmon resonance frequencies and damping rates for nanospheres. *Plasmonics* **2016**, *11* (3), 941-951.

66. Alabastri, A.; Tuccio, S.; Giugni, A.; Toma, A.; Liberale, C.; Das, G.; Angelis, F. D.; Fabrizio, E. D.; Zaccaria, R. P., Molding of plasmonic resonances in metallic nanostructures: Dependence of the non-linear electric permittivity on system size and temperature. *Materials* **2013**, *6* (11), 4879-4910.

67. Chen, P.; Tran, N. T.; Wen, X.; Xiong, Q.; Liedberg, B., Inflection Point of the localized surface plasmon resonance peak: A General method to improve the sensitivity. *ACS sensors* **2017**, *2* (2), 235-242.

68. Juvé, V.; Cardinal, M. F.; Lombardi, A.; Crut, A.; Maioli, P.; Pérez-Juste, J.; Liz-Marzán, L. M.; Del Fatti, N.; Vallée, F., Size-dependent surface plasmon resonance broadening in nonspherical nanoparticles: single gold nanorods. *Nano letters* **2013**, *13* (5), 2234-2240.

69. Tsalu, P. V.; Kim, G. W.; Hong, J. W.; Ha, J. W., Homogeneous localized surface plasmon resonance inflection points for enhanced sensitivity and tracking plasmon damping in single gold bipyramids. *Nanoscale* **2018**, *10* (26), 12554-12563.

70. Minjung Seo, J. W. H., Effective surface-enhanced Raman scattering of randomly branched gold nano-urchins with Rhodamine 6G as Raman reporters. *Microchemical Journal* **2018**, *140*, 47-51.

71. Allen, C. S.; Van Duyne, R. P., Molecular generality of surface-enhanced Raman spectroscopy (SERS). A detailed investigation of the hexacyanoruthenate ion adsorbed on silver and copper electrodes. *Journal of the American Chemical Society* **1981**, *103* (25), 7497-7501.

72. Bilić, A.; Reimers, J. R.; Hush, N. S., Adsorption of pyridine on the gold (111) surface: implications for "alligator clips" for molecular wires. *The Journal of Physical*

*Chemistry B* **2002**, *106* (26), 6740-6747.

73. Mollenhauer, D.; Gaston, N.; Voloshina, E.; Paulus, B., Interaction of pyridine derivatives with a gold (111) surface as a model for adsorption to large nanoparticles. *The Journal of Physical Chemistry C* **2013**, *117* (9), 4470-4479.

74. Tadjeddine, A.; Le Rille, A.; Pluchery, O.; Hebert, P.; Zheng, W.; Marin, T., Adsorption of pyridine on gold, studied by difference frequency generation (DFG) using the CLIO-FEL. *Nuclear Instruments and Methods in Physics Research Section A: Accelerators, Spectrometers, Detectors and Associated Equipment* **1999**, *429* (1-3), 481-484.

75. Dressler, D.; Mastai, Y.; Rosenbluh, M.; Fleger, Y., Surface-enhanced Raman spectroscopy as a probe for orientation of pyridine compounds on colloidal surfaces. *Journal of molecular structure* **2009**, *935* (1-3), 92-96.

76. Suzuki, T.; Hirooka, T.; Kondow, T.; Kuchitsu, K., Orientation of pyridine molecules adsorbed on silver surface as studied by penning ionization electron spectroscopy. *Surface Science* **1985**, *158* (1-3), 515-524.

77. Chase, S.; Bacsa, W.; Mitch, M.; Piloni, L.; Lannin, J., Surface-enhanced Raman scattering and photoemission of C 60 on noble-metal surfaces. *Physical Review B* **1992**, *46* (12), 7873.

78. Gao, P.; Weaver, M. J., Surface-enhanced Raman spectroscopy as a probe of adsorbate-surface bonding: benzene and monosubstituted benzenes adsorbed at gold electrodes. *The Journal of Physical Chemistry* **1985**, *89* (23), 5040-5046.

79. Aikens, C. M.; Schatz, G. C., TDDFT studies of absorption and SERS spectra of pyridine interacting with Au<sub>20</sub>. *The Journal of Physical Chemistry A* **2006**, *110* (49), 13317-13324.

80. Brolo, A.; Irish, D.; Lipkowski, J., Surface-enhanced Raman spectra of pyridine and pyrazine adsorbed on a Au (210) single-crystal electrode. *The Journal of Physical Chemistry B* **1997**, *101* (20), 3906-3909.

81. Gong, X.; Taszarek, M.; Schefzig, L.; Reissig, H.-U.; Thierbach, S.; Wassermann, B.; Graf, C.; Mollenhauer, D.; Ru<sup>hl</sup>, E., Adsorption of Mono- and Divalent 4-(Dimethylamino) pyridines on Gold Surfaces: Studies by Surface-Enhanced Raman Scattering and Density Functional Theory. *Langmuir* **2019**, *35* (26), 8667-8680.

82. Jeon, H. B.; Ha, J. W., Single-Particle Study: Plasmon Damping of Gold Nanocubes with Vertices by Adsorbate Molecules. *Bulletin of the Korean Chemical Society* **2018**, *39* (9), 1117-1119.

83. McFarland, A. D.; Van Duyne, R. P., Single silver nanoparticles as real-time optical

sensors with zeptomole sensitivity. *Nano letters* **2003**, 3 (8), 1057-1062.